

To catch and reverse a quantum jump mid-flight

Z.K. Minev,¹ S.O. Mundhada,¹ S. Shankar,¹ P. Reinhold,¹ R. Gutiérrez-Jáuregui,²
R.J. Schoelkopf,¹ M. Mirrahimi,^{3,4} H.J. Carmichael,² and M.H. Devoret¹

¹*Department of Applied Physics, Yale University,
New Haven, Connecticut 06511, USA*

²*The Dodd-Walls Centre for Photonic and Quantum Technologies,
Department of Physics, University of Auckland,
Private Bag 92019, Auckland, New Zealand*

³*Yale Quantum Institute, Yale University,
New Haven, Connecticut 06520, USA*

⁴*QUANTIC team, INRIA de Paris,
2 Rue Simone Iff, 75012 Paris, France*

(Dated: December 11, 2021)

A quantum system driven by a weak deterministic force while under strong continuous energy measurement exhibits quantum jumps between its energy levels¹⁻³. This celebrated phenomenon is emblematic of the special nature of randomness in quantum physics. The times at which the jumps occur are reputed to be fundamentally unpredictable. However, certain classical phenomena, like tsunamis, while unpredictable in the long term, may possess a degree of predictability in the short term, and in some cases it may be possible to prevent a disaster by detecting an advance warning signal. Can there be, despite the indeterminism of quantum physics, a possibility to know if a quantum jump is about to occur or not? In this paper, we answer this question affirmatively by experimentally demonstrating that the completed jump from the ground to an excited state of a superconducting artificial atom can be tracked, as it follows its predictable “flight,” by monitoring the population of an auxiliary level coupled to the ground state. Furthermore, we show that the completed jump is continuous, deterministic, and coherent. Exploiting this coherence, we catch and reverse a quantum jump mid-flight, thus preventing its completion. This real-time intervention is based on a particular lull period in the population of the auxiliary level, which serves as our advance warning signal. Our results, which agree with theoretical predictions essentially without adjustable parameters, support the modern quantum trajectory theory⁴⁻⁷ and provide new ground for the exploration of real-time intervention techniques in the control of quantum systems, such as early detection of error syndromes.

Bohr conceived of quantum jumps⁸ between energy levels in 1913, but it took seven decades until they were directly observed in a single atom¹⁻³. Since then, quantum jumps have been observed in a variety of atomic⁹⁻¹² and solid-state¹³⁻¹⁷ systems. Recently, quantum jumps have been recognized as an essential phenomenon in quantum feedback control^{18,19}, and in particular, for detecting and correcting decoherence-induced errors in quantum information systems^{20,21}.

Here, we focus on the canonical case of quantum jumps between two levels indirectly monitored by a third — the case that corresponds to the original observation of quantum jumps in atomic physics¹⁻³, see the level diagram of Fig. 1a. A surprising prediction emerges: according to quantum trajectory theory⁴, not only does the state of the system evolve con-

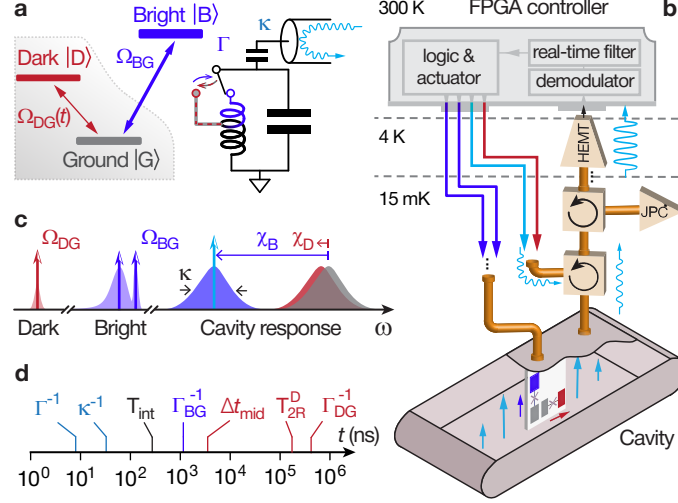


Figure 1. Principle of the experiment. **a**, Three level atom possessing a hidden transition (shaded region) between the ground $|G\rangle$ and dark $|D\rangle$ state, driven by a Rabi drive $\Omega_{DG}(t)$. Quantum jumps from $|G\rangle$ to $|D\rangle$ are indirectly monitored by a stronger Rabi drive between $|G\rangle$ and the bright state $|B\rangle$, whose occupancy is continuously monitored at rate Γ by an auxiliary oscillator (LC circuit on right), itself measured in reflection by a CW probe tone (light-blue wave). When the atom is in $|B\rangle$, the LC circuit frequency shifts to a lower value (effect schematically represented by switch). Therefore, the probe tone performs a $|B\rangle/\text{not-}|B\rangle$ measurement on the atom, and is blind to any superposition of $|G\rangle$ and $|D\rangle$. **b**, The actual atom used in the experiment is a superconducting circuit consisting of two strongly-hybridized transmon qubits placed inside a readout cavity at 15 mK. Control signals for the atom and cavity are supplied by a room-temperature field-programmable gate array (FPGA) controller. This fast electronics monitors the reflected signal from the cavity, and after demodulation and filtering, actuates the control signals. The amplifier chain includes circulators (curved arrows) and amplifiers (triangles and trapezoids). **c**, Frequency landscape of atom and cavity responses, overlaid with the control tones shown as vertical arrows. The cavity pull χ of the atom is nearly identical for $|G\rangle$ and $|D\rangle$, but markedly distinct for $|B\rangle$. The BG drive is bi-chromatic in order to address the bright transition independently of the cavity state. **d**, Hierarchy of timescales involved in the experiment, which are required to span 5 orders of magnitude, symbols explained in text (also, see Extended Data Table 1).

tinuously during the jump between the ground $|G\rangle$ and excited $|D\rangle$ state, but it is predicted that there is always a latency period prior to the jump, during which it is possible to acquire a signal that warns of the imminent occurrence of the jump (see Supplement). This advance warning signal consists of a rare, particular lull in the excitation of the ancilla state $|B\rangle$. The acquisition of this signal requires time-resolved detection of every photon emitted from $|B\rangle$, an almost unsurmountable problem in atomic physics²².

Instead, exploiting the specific advantages of superconducting artificial atoms and their quantum-limited readout chain, we designed an experiment that implements with maximum fidelity and minimum latency the detection of the advance warning signal occurring before

the quantum jump (see rest of Fig. 1).

First, we developed a superconducting artificial atom with the necessary V-shape level structure (see Fig. 1a and Methods). It consists, besides the ground level $|G\rangle$, of one protected, dark level $|D\rangle$ — engineered to not couple to any dissipative environment or any measurement apparatus — and one ancilla level $|B\rangle$, whose occupation is monitored at rate Γ . Quantum jumps between $|G\rangle$ and $|D\rangle$ are induced by a weak Rabi drive Ω_{DG} — although this drive might eventually be turned off during the jump, as explained later. Since a direct measurement of the dark level is not feasible, the jumps are monitored using the Dehmelt shelving scheme¹. Thus, the occupation of $|G\rangle$ is linked to that of $|B\rangle$ by the strong Rabi drive Ω_{BG} ($\Omega_{DG} \ll \Omega_{BG} \ll \Gamma$). In the atomic physics shelving scheme^{1–3}, an excitation to $|B\rangle$ is recorded by detecting the emitted photons from $|B\rangle$ with a photodetector. From the detection events — referred to in the following as “clicks” — one infers the occupation of $|G\rangle$. On the other hand, from the prolonged absence of clicks (to be defined precisely below), one infers that a quantum jump from $|G\rangle$ to $|D\rangle$ has occurred. Due to the poor collection efficiency and dead-time of photon counters in atomic physics²², it is exceedingly difficult to detect every individual click required to faithfully register the advance warning signal. However, superconducting systems present the advantage of high collection efficiencies^{23–29}, as their microwave photons are emitted into one-dimensional waveguides and are detected with the same quantum efficiencies as optical photons. Furthermore, rather than monitoring the direct fluorescence of the $|B\rangle$ state, we monitor its occupation by dispersively coupling it to an ancilla readout cavity. This gives us a way to counter-balance the residual inefficiency of our microwave photon detectors, as we now explain.

The readout cavity, schematically depicted in Fig. 1a by an LC circuit, is resonant at $\omega_C = 8979.64$ MHz and cooled to 15 mK. Its dispersive coupling to the atom results in a conditional shift of its resonance frequency by $\chi_B/2\pi = -5.08 \pm 0.2$ MHz ($\chi_D/2\pi = -0.33 \pm 0.08$ MHz) when the atom is in $|B\rangle$ ($|D\rangle$), see Fig. 1c. The engineered large asymmetry between χ_B and χ_D together with the cavity coupling rate to the output waveguide, $\kappa/2\pi = 3.62 \pm 0.05$ MHz, renders the cavity response markedly resolving for $|B\rangle$ vs. not- $|B\rangle$, yet non-resolving^{24,27,30} for $|G\rangle$ vs. $|D\rangle$, thus preventing information about the dark transition from reaching the environment. When probing the cavity response at $\omega_C - \chi_B$, the cavity either remains empty, when the atom is in $|G\rangle$ or $|D\rangle$, or fills with $\bar{n} = 5 \pm 0.2$ photons when the atom is in $|B\rangle$. This readout scheme yields a transduction of the $|B\rangle$ -occupancy signal with five-

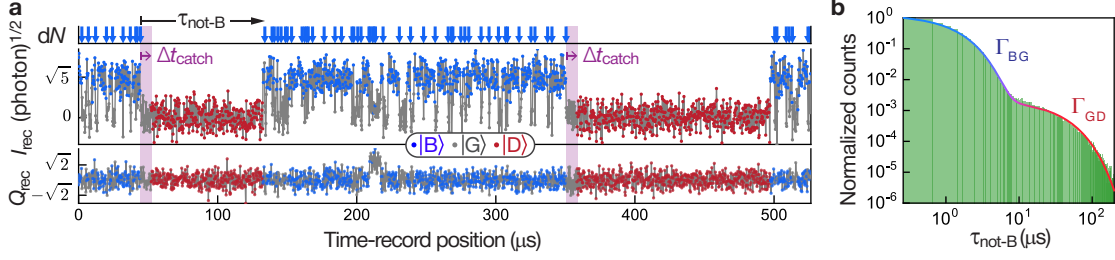


Figure 2. Unconditioned monitoring of quantum jumps in the 3-level system. **a**, Typical measurement of quadratures I_{rec} and Q_{rec} of signal reflected from readout cavity as a function of time. The color of the dots (see legend) denotes the state of the atom estimated by a real-time filter implemented with the FPGAs (see Methods). On top, the vertical arrows indicate “click” events (dN) corresponding to the inferred state changing from $|B\rangle$ to not- $|B\rangle$. The symbol $\tau_{\text{not-B}}$ corresponds to the time spent in not- $|B\rangle$, which is the time between two clicks minus the last duration spent in $|B\rangle$. An advance warning that a jump to $|D\rangle$ is occurring is triggered when *no* click has been observed for a duration Δt_{catch} , which is chosen between 1 and 12 μs at the start of the experiment. **b**, Log-log plot of the histogram of $\tau_{\text{not-B}}$ (shaded green) for 3.2 s of continuous data of the type of panel (a). Solid line is a bi-exponential fit defining jump rates $\Gamma_{\text{BG}} = (0.99 \pm 0.06 \mu\text{s})^{-1}$ and $\Gamma_{\text{GD}} = (30.8 \pm 0.4 \mu\text{s})^{-1}$.

fold amplification, which is an important advantage to overcome the noise of the following amplification stages. To summarize, in this readout scheme, the cavity probe inquires: Is the atom in $|B\rangle$ or not? The time needed to arrive at an answer with a confidence level of 68% (signal-to-noise ratio of 1) is $\Gamma^{-1} \approx 1/(\kappa\bar{n}) = 8.8$ ns for an ideal amplifier chain (see Supplement).

Importantly, the engineered near-zero coupling between the cavity and the $|D\rangle$ state protects the $|D\rangle$ state from harmful effects, including Purcell relaxation, photon shot-noise dephasing, and the yet essentially unexplained residual measurement-induced relaxation in superconducting qubits³¹. We have measured the following coherence times for the $|B\rangle$ state: energy relaxation $T_1^{\text{D}} = 116 \pm 5 \mu\text{s}$, Ramsey coherence $T_{2\text{R}}^{\text{D}} = 120 \pm 5 \mu\text{s}$, and Hahn echo $T_{2\text{E}}^{\text{D}} = 162 \pm 6 \mu\text{s}$. While protected, the $|D\rangle$ state is indirectly quantum-non-demolition (QND) read out by the combination of the V-structure, the drive between $|G\rangle$ and $|B\rangle$, and the fast $|B\rangle$ -state monitoring. In practice, we can access the population of $|D\rangle$ using an 80 ns unitary rotation followed by a projective measurement of $|B\rangle$ (see Methods).

Once the state of the readout cavity is imprinted with information about the occupation of $|B\rangle$, photons leak through the cavity output port into a superconducting waveguide, which is connected to the amplification chain, see Fig. 1b, where they are amplified by a factor of 10^{12} . The first stage of amplification is a quantum-limited Josephson parametric

converter (JPC)³², which is followed by a high-electron-mobility transistor (HEMT) amplifier at 4 K. The overall quantum efficiency of the amplification chain is $\eta = 0.33 \pm 0.03$ (see Methods). At room temperature, the heterodyne signal is demodulated by a home-built field-programmable gate array (FPGA) controller, with a 4 ns clock period for logic operations. The measurement record consists of a time series of two quadrature outcomes, I_{rec} and Q_{rec} , every 260 ns, which is the integration time T_{int} , from which the FPGA controller estimates the state of the atom in real time. To reduce the influence of noise, the controller applies a real-time, hysteretic IQ filter (see Methods), and then, from the estimated atom state, the control drives of the atom and readout cavity are actuated, realizing feedback control.

Having described the setup of the experiment, we proceed to report its results. The field reflected out of the cavity is monitored in a free-running protocol, for which the atom is subject to the continuous Rabi drives Ω_{BG} and Ω_{DG} , as depicted in Fig. 1. Figure 2a shows a typical trace of the measurement record, displaying the quantum jumps of our three-level artificial atom. For most of the displayed duration of the record, I_{rec} switches rapidly between a low and high value, corresponding to approximately 0 ($|G\rangle$ or $|D\rangle$) and 5 ($|B\rangle$) photons in the cavity, respectively. The spike in Q_{rec} at $t = 210 \mu\text{s}$ is recognized by the FPGA logic as a short-lived excursion of the atom to a higher excited state (Methods). The corresponding state of the atom, estimated by the FPGA controller, is depicted by the color of the dots. A change from $|B\rangle$ to not- $|B\rangle$ is equivalent to a “click” event, in that it corresponds to the emission of a photon from $|B\rangle$ to $|G\rangle$, whose occurrence time is shown by the vertical arrows in the inferred record $dN(t)$ (top). We could also indicate upward transitions from $|G\rangle$ to $|B\rangle$, corresponding to photon absorption events (not emphasized here), which would not be detectable in the atomic case.

In the record, the detection of clicks stops completely at $t = 45 \mu\text{s}$, which reveals a quantum jump from $|G\rangle$ to $|D\rangle$. The state $|D\rangle$ survives for $90 \mu\text{s}$ before the atom returns to $|G\rangle$ at $t = 135 \mu\text{s}$, when the rapid switching between $|G\rangle$ and $|B\rangle$ resumes until a second quantum jump to the dark state occurs at $t = 350 \mu\text{s}$. Thus, the record presents jumps from $|G\rangle$ to $|D\rangle$ in the form of click interruptions.

In Fig. 2b, which is based on the continuous tracking of the quantum jumps for 3.2 s, a histogram of the time spent in not- $|B\rangle$, $\tau_{\text{not-B}}$, is shown. The panel also shows a fit of the histogram by a bi-exponential curve that models two interleaved Poisson processes. This yields the average time the atom rests in $|G\rangle$ before an excitation to $|B\rangle$, $\Gamma_{\text{BG}}^{-1} = 0.99 \pm 0.06 \mu\text{s}$,

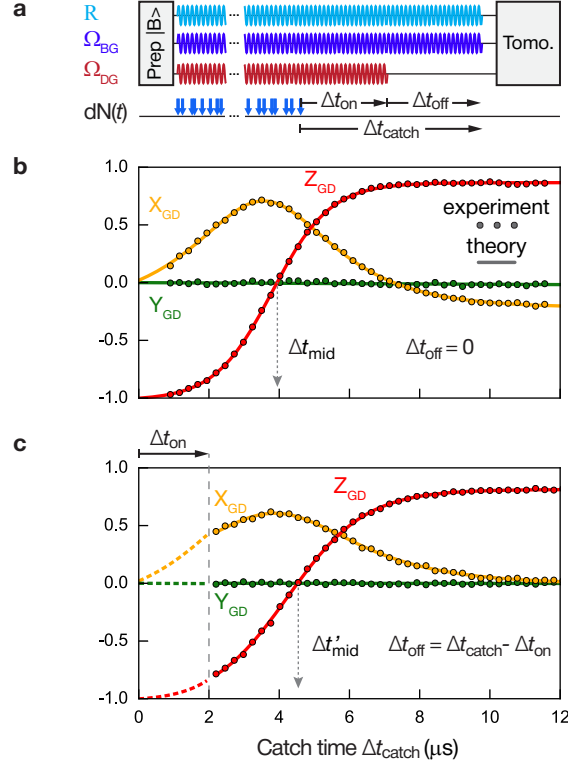


Figure 3. Catching the quantum jump mid-flight. **a**, The atom is initially prepared in $|B\rangle$. The readout tone (R) and atom Rabi drive Ω_{BG} are turned on until the catch condition is fulfilled, consisting of the detection of a click followed by the absence of click detections for a total time Δt_{catch} . The Rabi drive Ω_{DG} starts with Ω_{BG} , but can be shut off prematurely, prior to the end of Δt_{catch} . A tomography measurement is performed after Δt_{catch} . **b & c**, Conditional tomography revealing the continuous, coherent, and, surprisingly, deterministic flight (when completed) of the quantum jump from $|G\rangle$ to $|D\rangle$. The mid-flight time Δt_{mid} is defined by $Z_{\text{GD}} = 0$. The jump proceeds even when Ω_{DG} is turned off at the beginning of the flight (panel c), $\Delta t_{\text{on}} = 2 \mu\text{s}$. Data obtained from 6.8×10^6 experimental realizations. Solid lines: theoretical prediction. Dashed lines in panel c: theory curves for the Δt_{on} interval, reproduced from panel b. Theory curves of panel b reproduced as dashed lines in panel c. The data suggests that an advance-warning signal of the jump can be provided by a no-click period for catch time $\Delta t_{\text{catch}} = \Delta t_{\text{mid}}$, at which half of the jumps will complete.

and the average time the atom stays up in $|D\rangle$ before returning to $|G\rangle$ and being detected, $\Gamma_{\text{GD}}^{-1} = 30.8 \pm 0.4 \mu\text{s}$. The average time between two consecutive $|G\rangle$ to $|D\rangle$ jumps is $\Gamma_{\text{DG}}^{-1} = 220 \pm 5 \mu\text{s}$. The corresponding rates depend on the atom drive amplitudes (Ω_{DG} and Ω_{BG}) and the measurement rate Γ (see Supplement). Crucially, all the rates in the system must be distributed over a minimum of 5 orders of magnitude, as shown in Fig. 1d.

Having observed the quantum jumps in the free-running protocol, we proceed to conditionally actuate the system control tones in order to tomographically reconstruct the time

dynamics of the quantum jump from $|G\rangle$ to $|D\rangle$, see Fig. 3a. Like previously, after initiating the atom in $|B\rangle$, the FPGA controller continuously subjects the system to the atom drives (Ω_{BG} and Ω_{DG}) and to the readout tone (R). However, in the event that the controller detects a single click followed by the complete absence of clicks for a total time Δt_{catch} , the controller suspends all system drives, thus freezing the system evolution, and performs tomography, as explained in Methods. Note that in each realization, the tomography measurement yields a single +1 or -1 outcome, one bit of information for a single density matrix component. We also introduce a division of the duration Δt_{catch} into two phases, one lasting Δt_{on} during which Ω_{DG} is left on and one lasting $\Delta t_{\text{off}} = \Delta t_{\text{catch}} - \Delta t_{\text{on}}$ during which Ω_{DG} is turned off. As we explain below, this has the purpose of demonstrating that the evolution of the jump is not simply due to the Rabi drive between $|G\rangle$ and $|D\rangle$.

In Fig. 3b, we show the dynamics of the jump mapped out in the full presence of the Rabi drive, Ω_{GD} , by setting $\Delta t_{\text{off}} = 0$. From 3.4×10^6 experimental realizations we reconstruct, as a function of Δt_{catch} , the quantum state, and present the evolution of the jump from $|G\rangle$ to $|D\rangle$ as the normalized, conditional GD tomogram (Methods). For $\Delta t_{\text{catch}} < 2 \mu\text{s}$, the atom is predominantly detected in $|G\rangle$ ($Z_{GD} = -1$), whereas for $\Delta t_{\text{catch}} > 10 \mu\text{s}$, it is predominantly detected in $|D\rangle$ ($Z_{GD} = +1$). Imperfections, due to excitations to higher levels, reduce the maximum observed value to $Z_{GD} = +0.9$ (Supplement).

For intermediate no-click times, between $\Delta t_{\text{catch}} = 2 \mu\text{s}$ and $\Delta t_{\text{catch}} = 10 \mu\text{s}$, the state of the atom evolves continuously and coherently from $|G\rangle$ to $|D\rangle$ — the flight of the quantum jump. The time of mid flight, $\Delta t_{\text{mid}} \equiv 3.95 \mu\text{s}$, is markedly shorter than the Rabi period $2\pi/\Omega_{DG} = 50 \mu\text{s}$, and is given by the function $\Delta t_{\text{mid}} = \left(\frac{\Omega_{BG}^2}{2\Gamma}\right)^{-1} \ln\left(\frac{\Omega_{BG}^2}{\Omega_{DG}\Gamma} + 1\right)$, in which Ω_{DG} enters logarithmically (see Supplement). The maximum coherence of the superposition, corresponding to $\sqrt{X_{GD}^2 + Y_{GD}^2}$, during the flight is 0.71 ± 0.005 , quantitatively understood to be limited by several small imperfections (Supplement).

Motivated by the exact quantum trajectory theory, we fit the experimental data with the analytic form of the jump evolution, $Z_{GD}(\Delta t_{\text{catch}}) = a + b \tanh(\Delta t_{\text{catch}}/\tau + c)$, $X_{GD}(\Delta t_{\text{catch}}) = a' + b' \text{sech}(\Delta t_{\text{catch}}/\tau' + c')$, and $Y_{GD}(\Delta t_{\text{catch}}) = 0$. We compare the fitted jump parameters ($a, a', b, b', c, c', \tau, \tau'$) to those calculated from the theory and numerical simulations using independently measured system characteristics (Supplement).

By repeating the experiment with $\Delta t_{\text{on}} = 2 \mu\text{s}$, in Fig. 3c, we show that the jump proceeds even if the GD drive is shut off at the beginning of the no-click period. The jump remains

coherent and only differs from the previous case in a minor renormalization of the overall amplitude and timescale. The mid-flight time of the jump, $\Delta t'_{\text{mid}}$, is given by an updated formula (see Supplement). The results demonstrate that the role of the Rabi drive Ω_{DG} is to initiate the jump and provide a reference for the phase of its evolution³³.

Note that the $\Delta t_{\text{catch}} \gg \Delta t_{\text{mid}}$ non-zero steady state value of X_{GD} in Fig. 3b is the result of the competition between the Rabi drive Ω_{DG} and the effect of the measurement of $|B\rangle$ (see Supplement). This is confirmed in Fig. 3c, where $\Omega_{\text{DG}} = 0$, and where there is no offset in the steady state value.

The results of Fig. 3 demonstrate that despite the unpredictability of the jumps from $|G\rangle$ to $|D\rangle$, they are preceded by an identical no-click record. While the jump starts at a random time and can be prematurely interrupted by a click, the deterministic nature of the flight comes as a surprise given the quantum fluctuations in the heterodyne record I_{rec} during the jump — an island of predictability in a sea of uncertainty.

In Fig. 4b, we show that by choosing $\Delta t_{\text{catch}} = \Delta t_{\text{mid}}$ for the no-click period to serve as an advance warning signal, we reverse the quantum jump³⁴ in the presence of Ω_{DG} ; the same result is found when Ω_{DG} is off, see Extended Results. The reverse pulse characteristics are defined in Fig. 4a. For $\varphi_I = \pi/2$, our feedback protocol succeeds in reversing the jump to $|G\rangle$ with $83.1\% \pm 0.3\%$ fidelity, while for $\varphi_I = 3\pi/2$, the protocol completes the jump to $|D\rangle$, with $82.0\% \pm 0.3\%$ fidelity. In a control experiment, we repeat the protocol by applying the reverse pulse at random times, rather than those determined by the advance warning signal. Without the advance warning signal, the measured populations only reflect those of the ensemble average.

In a final experiment, we programmed the controller with the optimal reverse pulse parameters $\{\theta_I(\Delta t_{\text{catch}}), \varphi_I(\Delta t_{\text{catch}})\}$, and as shown in Fig. 4c, we measured the success of the reverse protocol as a function of the catch time, Δt_{catch} . The closed/open dots indicate the results for Ω_{DG} on/off, while the solid curves are theory fits motivated by the exact analytic expressions (Supplement). The complementary red dots and curves reproduce the open-loop results of Fig. 3 for comparison. The excellent agreement between experiment and theory including known experimental imperfections provides (see Supplement) support to the modern quantum trajectory theory and its reliability for predicting the performance of real-time intervention techniques in the control of quantum systems.

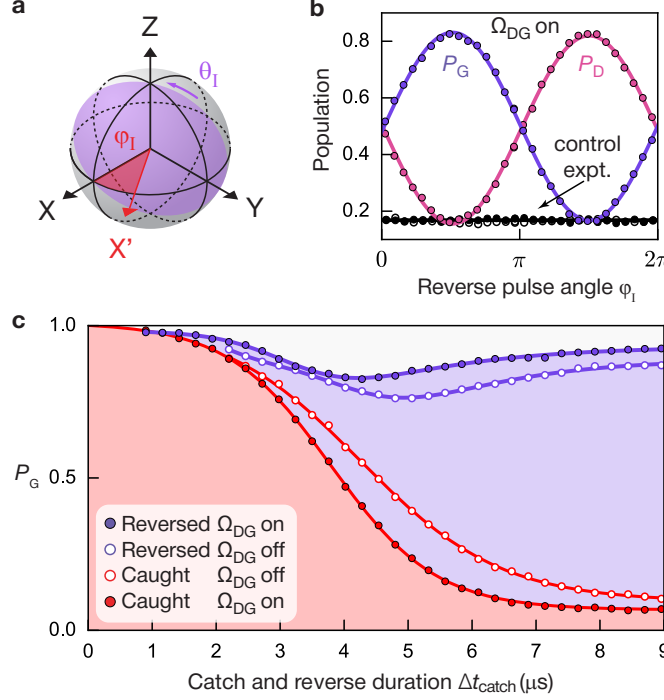


Figure 4. Reversing the quantum jump mid-flight. **a**, Bloch sphere of the GD manifold, showing the axis X' for the jump reversal, defined by the azimuthal angle φ_I . The angle of the intervention pulse is θ_I . **b**, Success probabilities P_G (purple) and P_D (orange) to reverse to $|G\rangle$ and complete to $|D\rangle$ the quantum jump mid-flight at $\Delta t_{\text{catch}} = \Delta t_{\text{mid}}$, with $\theta_I = \pi/2$, in the presence of the Rabi drive Ω_{DG} . Black dots: success probability for $|G\rangle$ (closed dots) and $|D\rangle$ (open dots) in a control experiment where intervention is applied at random times along the record, rather than at Δt_{catch} . **c**, Optimal success of reverse protocol (purple) as a function of Δt_{catch} . The FPGA controller is programmed with the optimal $\{\theta_I(\Delta t_{\text{catch}}), \varphi_I(\Delta t_{\text{catch}})\}$. Closed and open dots correspond to $\Delta t_{\text{on}} = \Delta t_{\text{catch}}$ and $\Delta t_{\text{on}} = 2\mu\text{s}$, respectively. Red points show the corresponding open-loop (no intervention) results from Fig. 3b and c.

I. METHODS SUMMARY

Atom-cavity implementation. The superconducting artificial atom consisted of two coupled transmon qubits fabricated on a 2.9 mm-by-7 mm double-side-polished c-plane sapphire wafer with the Al/ AlO_x /Al bridge-free electron-beam lithography technique^{35,36}. The first transmon (B) was aligned with the electric field of the fundamental TE_{101} mode of an aluminum rectangular cavity (alloy 6061; dimensions: 5.08 mm by 35.5 mm by 17.8 mm), while the second transmon (D) was oriented perpendicular to the first and positioned $170\mu\text{m}$ adjacent to it. The inductance of the Josephson junction of each transmon (9 nH for both B and D), the placement and dimensions of each transmon, and the geometry of the cavity were designed and optimized using finite-element electromagnetic analysis and the energy-

participation-ratio (EPR) method³⁷. The analysis also verified that the coupling between the two qubits is described by the Hamiltonian $\hat{H}_{\text{int}} = -\chi_{\text{DB}}\hat{n}_{\text{B}} \otimes \hat{n}_{\text{D}}$, where $\hat{n}_{\text{B/D}}$ is the photon number operator of the B/D qubit, and χ_{DB} is the cross-Kerr frequency.

The measured frequency and anharmonicity of the D qubit were $\omega_{\text{D}}/2\pi = 4845.255$ MHz and $\alpha_{\text{DG}}/2\pi = 152$ MHz, respectively, while those of the B qubit were $\omega_{\text{B}}/2\pi = 5570.349$ MHz and $\alpha_{\text{BG}}/2\pi = 195$ MHz, respectively. The cross-Kerr coupling was $\chi_{\text{DB}}/2\pi = 61$ MHz. The relaxation time of $|B\rangle$ was $T_1^{\text{B}} = 28 \pm 2 \mu\text{s}$, limited by the Purcell effect by design, while its Ramsey coherence time was $T_{2\text{R}}^{\text{B}} = 18 \pm 1 \mu\text{s}$. The remaining parameters of the system are provided in the main text.

Atom and cavity drives. In all experiments, the following drive parameters were used: The DG Rabi drive, Ω_{DG} , was applied 275 kHz below ω_{D} , to account for the Stark shift of the cavity. The BG drive, Ω_{BG} , was realized as a bi-chromatic tone in order to unselectively address the BG transition, which was broadened and Stark shifted due to the coupling between $|B\rangle$ and the readout cavity. Specifically, we address transitions from $|G\rangle$ to $|B\rangle$ with a Rabi drive $\Omega_{\text{B0}}/2\pi = 1.20 \pm 0.01$ MHz at frequency ω_{BG} , whereas transitions from $|B\rangle$ to $|G\rangle$ are addressed with a Rabi drive $\Omega_{\text{B1}}/2\pi = 0.60 \pm 0.01$ MHz tuned 30 MHz below ω_{BG} . This bi-chromatic scheme provided the ability to tune the up-click and down-click rates independently, but otherwise essentially functioned as an incoherent broad-band source.

IQ filter. To mitigate the effects of imperfections in the atom readout scheme in extracting a $|B\rangle/\text{not-}|B\rangle$ result, we applied a two-point, hysteretic IQ filter, implemented on the FPGA controller in real time. The filter is realized by comparing the present quadrature record values $\{I_{\text{rec}}, Q_{\text{rec}}\}$, with three thresholds (I_{B} , $I_{\bar{\text{B}}}$, and Q_{B}) in the following way:

Input:	$Q_{\text{rec}} \geq Q_{\text{B}}$ or $I_{\text{rec}} > I_{\text{B}}$	$Q_{\text{rec}} < Q_{\text{B}}$ and $I_{\text{rec}} < I_{\bar{\text{B}}}$	$Q_{\text{rec}} < Q_{\text{B}}$ and $I_{\bar{\text{B}}} \leq I_{\text{rec}} \leq I_{\text{B}}$
Output:	$ B\rangle$	not- $ B\rangle$	previous

The filter and thresholds were selected to provide a best estimate of the time of a click, operationally understood as a change in the filter output from $|B\rangle$ to not- $|B\rangle$. The I_{B} and $I_{\bar{\text{B}}}$ thresholds were chosen 1.5 standard deviations away from the I-quadrature mean of the $|B\rangle$ and not- $|B\rangle$ distributions, respectively. The Q_{B} threshold was chosen 3 standard deviations away from the Q-quadrature mean. Higher excited states of the atom were selected out by Q_{rec} values exceeding the Q_{B} threshold.

Tomography. At the end of each experimental realization, we performed one of 15 rotation sequences on the atom that transferred information about one component of the

density matrix, $\hat{\rho}_a$, to the population of $|B\rangle$, which was measured with a 600 ns square pulse on the readout cavity. Pulses were calibrated with a combination of Rabi, derivative removal via adiabatic gate (DRAG)³⁸, All-XY³⁹, and amplitude pulse train sequences⁴⁰. The readout signal was demodulated with the appropriate digital filter function required to realize temporal mode matching⁴¹. To remove the effect of potential systematic offset errors in the readout signal, we subtracted the measurement results of operator components of $\hat{\rho}_a$ and their opposites. From the measurement results of this protocol, we reconstructed the density matrix $\hat{\rho}_a$, and subsequently parametrized it in the useful form

$$\hat{\rho}_a = \begin{pmatrix} \frac{N}{2}(1 - Z_{GD}) & \frac{N}{2}(X_{GD} + iY_{GD}) & R_{BG} + iI_{BG} \\ \frac{N}{2}(X_{GD} - iY_{GD}) & \frac{N}{2}(1 + Z_{GD}) & R_{BD} + iI_{BD} \\ R_{BG} - iI_{BG} & R_{BD} - iI_{BD} & 1 - N \end{pmatrix},$$

where X_{GD} , Y_{GD} , and Z_{GD} are the Bloch vector components of the GD manifold, N is the total population of the $|G\rangle$ and $|D\rangle$ states, while R_{BG} , R_{BD} , I_{BG} and I_{BD} are the coherences associated with $|B\rangle$, relative to the GD manifold. The measured population in $|B\rangle$, $1 - N$, remains below 0.03 during the quantum jump, see Extended Data Fig. 4. Tomographic reconstruction was calibrated and verified by preparing Clifford states, accounting for the readout fidelity of 97%.

ACKNOWLEDGEMENTS

Z.K.M. acknowledges fruitful discussion with S.M. Girvin, M.P. Silveri, and V.V. Albert. V.V. Albert addressed one aspect of the Lindblad theoretical modeling regarding the waiting-time distribution. Facilities use was supported by the Yale Institute for Nanoscience and Quantum Engineering (YINQE), the Yale SEAS cleanroom, and NSF MRSEC DMR 1119826. This research was supported by ARO under Grant No. W911NF-14-1-0011. R.G.J. and H.J.C. acknowledge support from the Marsden fund of the Royal Society of New Zealand.

AUTHOR CONTRIBUTIONS

Z.K.M. conceived the experiment based on theoretical predictions by H.J.C., implemented the experiment, and analyzed the data. H.J.C. and R.G.J. performed the theoretical model-

ing and numerical simulations. S.O.M. contributed to the design of the device, and with S.S. to its fabrication. P.R. and R.J.S. assisted with the FPGA. M.M. contributed theoretical support, and M.H.D. supervised the project. Z.K.M. and M.H.D. wrote the manuscript, and H.J.C. contributed the theoretical supplement. All authors provided suggestions for the experiment, discussed the results and contributed to the manuscript.

CORRESPONDENCE

Correspondence and requests for materials should be addressed to Z.K. Minev (email: zlatko.minev@yale.edu)⁴² and M.H. Devoret (email: michel.devoret@yale.edu)

DATA AVAILABILITY

The data that support the findings of this study are available from the corresponding authors on reasonable request.

-
- ¹ Warren Nagourney, Jon Sandberg, and Hans Dehmelt, “Shelved optical electron amplifier: Observation of quantum jumps,” *Physical Review Letters* **56**, 2797–2799 (1986).
- ² Th. Sauter, W Neuhauser, R Blatt, and P E Toschek, “Observation of Quantum Jumps,” *Physical Review Letters* **57**, 1696–1698 (1986).
- ³ J C Bergquist, Randall G Hulet, Wayne M Itano, and D J Wineland, “Observation of Quantum Jumps in a Single Atom,” *Physical Review Letters* **57**, 1699–1702 (1986).
- ⁴ Howard J. Carmichael, *An Open Systems Approach to Quantum Optics* (Springer, Berlin, Heidelberg, 1993).
- ⁵ C W Gardiner, A S Parkins, and P Zoller, “Wave-function quantum stochastic differential equations and quantum-jump simulation methods,” *Physical Review A* **46**, 4363–4381 (1992).
- ⁶ Jean Dalibard, Yvan Castin, and Klaus Mølmer, “Wave-function approach to dissipative processes in quantum optics,” *Physical Review Letters* **68**, 580–583 (1992).
- ⁷ Alexander N Korotkov, “Continuous quantum measurement of a double dot,” *Physical Review B* **60**, 5737–5742 (1999).
- ⁸ Niels Bohr, “On the Constitution of Atoms and Molecules,” *Philosophical Magazine* **26**, 476–502 (1913).
- ⁹ Th. Basche, S Kummer, and C Brauchle, “Direct spectroscopic observation of quantum jumps of a single molecule,” *Nature* **373**, 132–134 (1995).
- ¹⁰ S. Peil and G. Gabrielse, “Observing the Quantum Limit of an Electron Cyclotron: QND Measurements of Quantum Jumps between Fock States,” *Physical Review Letters* **83**, 1287–1290 (1999).
- ¹¹ Sébastien Sebastian Gleyzes, Stefan Kuhr, Christine Guerlin, Julien Bernu, Samuel Deléglise, Ulrich Busk, Michel Brune, Jean-Michel Raimond, Serge Haroche, Samuel Deleglise, Ulrich Busk Hoff, Michel Brune, Jean-Michel Raimond, and Serge Haroche, “Observing the quantum jumps of light : birth and death of a photon in a cavity,” *Nature* **446**, 297 (2007).
- ¹² Christine Guerlin, Julien Bernu, Samuel Deléglise, Clément Sayrin, Sébastien Gleyzes, Stefan Kuhr, Michel Brune, Jean-Michel Raimond, and Serge Haroche, “Progressive field-state collapse and quantum non-demolition photon counting.” *Nature* **448**, 889–93 (2007), arXiv:0707.3880.

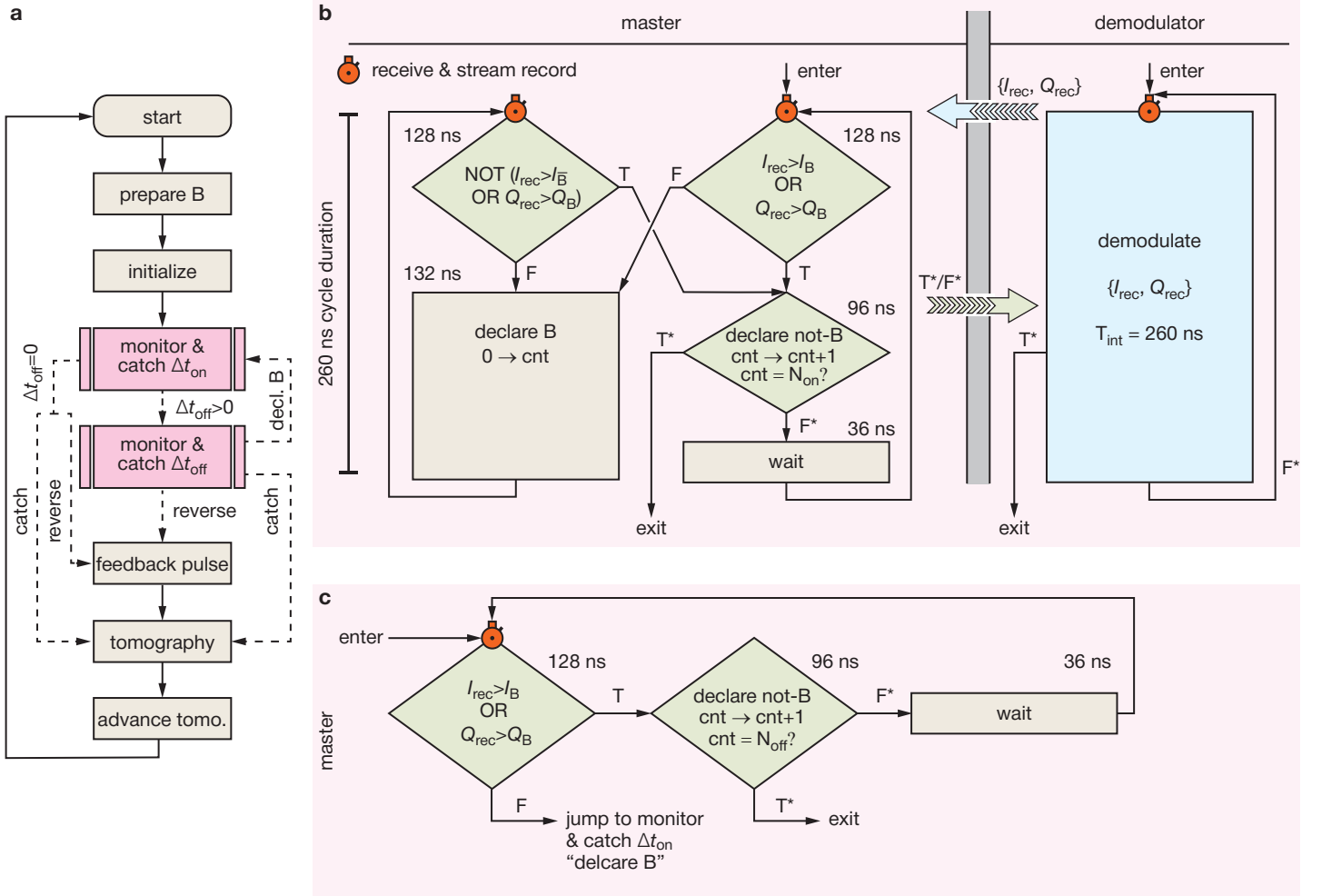
- ¹³ F. Jelezko, I. Popa, A. Gruber, C. Tietz, J. Wrachtrup, A. Nizovtsev, and S. Kilin, “Single spin states in a defect center resolved by optical spectroscopy,” *Applied Physics Letters* **81**, 2160–2162 (2002).
- ¹⁴ Philipp Neumann, Johannes Beck, Matthias Steiner, Florian Rempp, Helmut Fedder, Philip R. Hemmer, Jörg Wrachtrup, and Fedor Jelezko, “Single-Shot Readout of a Single Nuclear Spin,” *Science* **329**, 542–544 (2010).
- ¹⁵ Lucio Robledo, Lilian Childress, Hannes Bernien, Bas Hensen, Paul F. A. Alkemade, and Ronald Hanson, “High-fidelity projective read-out of a solid-state spin quantum register,” *Nature* **477**, 574–578 (2011), arXiv:1301.0392v1.
- ¹⁶ R. Vijay, D. H. Slichter, and I. Siddiqi, “Observation of Quantum Jumps in a Superconducting Artificial Atom,” *Physical Review Letters* **106**, 110502 (2011), arXiv:1009.2969.
- ¹⁷ M. Hatridge, S. Shankar, M. Mirrahimi, F. Schackert, K. Geerlings, T. Brecht, K. M. Sliwa, B. Abdo, L. Frunzio, S. M. Girvin, R. J. Schoelkopf, and M. H. Devoret, “Quantum Back-Action of an Individual Variable-Strength Measurement,” *Science* **339**, 178–181 (2013).
- ¹⁸ Samuel Deléglise, Igor Dotsenko, Clément Sayrin, Julien Bernu, Michel Brune, Jean-Michel Raimond, and Serge Haroche, “Reconstruction of non-classical cavity field states with snapshots of their decoherence,” *Nature* **455**, 510–514 (2008), arXiv:0809.1064.
- ¹⁹ Clément Sayrin, Igor Dotsenko, Xingxing Zhou, Bruno Peaudecerf, Théo Rybarczyk, Sébastien Gleyzes, Pierre Rouchon, Mazhar Mirrahimi, Hadis Amini, Michel Brune, Jean-Michel Raimond, and Serge Haroche, “Real-time quantum feedback prepares and stabilizes photon number states,” *Nature* **477**, 73–77 (2011), arXiv:1107.4027.
- ²⁰ L. Sun, A. Petrenko, Z. Leghtas, B. Vlastakis, G. Kirchmair, K. M. Sliwa, A. Narla, M. Hatridge, S. Shankar, J. Blumoff, L. Frunzio, M. Mirrahimi, M. H. Devoret, and R. J. Schoelkopf, “Tracking Photon Jumps with Repeated Quantum Non-Demolition Parity Measurements,” *Nature* **511**, 444–448 (2013), arXiv:1311.2534.
- ²¹ Nissim Ofek, Andrei Petrenko, Reinier Heeres, Philip Reinhold, Zaki Leghtas, Brian Vlastakis, Yehan Liu, Luigi Frunzio, S. M. Girvin, Liang Jiang, Mazhar Mirrahimi, M. H. Devoret, and R. J. Schoelkopf, “Demonstrating Quantum Error Correction that Extends the Lifetime of Quantum Information,” *Nature* **536**, 441–445 (2016), arXiv:1602.04768.
- ²² Jurgen Volz, Roger Gehr, Guilhem Dubois, Jerome Esteve, and Jakob Reichel, “Measurement of the internal state of a single atom without energy exchange,” *Nature* **475**, 210–213 (2011).

- ²³ R. Vijay, C. Macklin, D. H. Slichter, S. J. Weber, K. W. Murch, R. Naik, A. N. Korotkov, and I. Siddiqi, “Stabilizing Rabi oscillations in a superconducting qubit using quantum feedback,” *Nature* **490**, 77–80 (2012), arXiv:1205.5591.
- ²⁴ D. Ristè, M. Dukalski, C. A. Watson, G. de Lange, M. J. Tiggelman, Ya. M. Blanter, K. W. Lehnert, R. N. Schouten, and L. DiCarlo, “Deterministic entanglement of superconducting qubits by parity measurement and feedback,” *Nature* **502**, 350–354 (2013).
- ²⁵ K. W. Murch, S. J. Weber, K. M. Beck, E. Ginossar, and I. Siddiqi, “Reduction of the radiative decay of atomic coherence in squeezed vacuum,” *Nature* **499**, 62–65 (2013), arXiv:1301.6276.
- ²⁶ S. J. Weber, A. Chantasri, J. Dressel, A. N. Jordan, K. W. Murch, and I. Siddiqi, “Mapping the optimal route between two quantum states,” *Nature* **511**, 570–573 (2014), arXiv:1403.4992.
- ²⁷ N. Roch, M. E. Schwartz, F. Motzoi, C. Macklin, R. Vijay, A. W. Eddins, A. N. Korotkov, K. B. Whaley, M. Sarovar, and I. Siddiqi, “Observation of measurement-induced entanglement and quantum trajectories of remote superconducting qubits,” *Physical Review Letters* **112**, 170501 (2014), arXiv:1402.1868.
- ²⁸ G. De Lange, D. Riste, M. J. Tiggelman, C. Eichler, L. Tornberg, G. Johansson, A. Wallraff, R. N. Schouten, and L. Dicarlo, “Reversing quantum trajectories with analog feedback,” *Physical Review Letters* **112**, 080501 (2014), arXiv:1311.5472.
- ²⁹ P. Campagne-Ibarcq, P. Six, L. Bretheau, A. Sarlette, M. Mirrahimi, P. Rouchon, and B. Huard, “Observing Quantum State Diffusion by Heterodyne Detection of Fluorescence,” *Physical Review X* **6**, 011002 (2016), arXiv:1511.01415.
- ³⁰ J. M. Gambetta, A. A. Houck, and Alexandre Blais, “Superconducting Qubit with Purcell Protection and Tunable Coupling,” *Physical Review Letters* **106**, 030502 (2011), arXiv:1009.4470.
- ³¹ D H Slichter, C Müller, R Vijay, S J Weber, A Blais, and I Siddiqi, “Quantum Zeno effect in the strong measurement regime of circuit quantum electrodynamics,” *New Journal of Physics* **18**, 53031 (2016).
- ³² N. Bergeal, F. Schackert, M. Metcalfe, R. Vijay, V. E. Manucharyan, L. Frunzio, D. E. Prober, R. J. Schoelkopf, S. M. Girvin, and M. H. Devoret, “Phase-preserving amplification near the quantum limit with a Josephson ring modulator,” *Nature* **465**, 64–68 (2010), arXiv:0912.3407.
- ³³ A similar phase reference for a non-unitary, yet deterministic, evolution induced by measurement was previously found in a different context in: N. Katz, M. Ansmann, R. C. Bialczak, E. Lucero, R. McDermott, M. Neeley, M. Steffen, E. M. Weig, A. N. Cleland, J. M. Martinis, and A. N.

- Korotkov, Science (New York, N.Y.) 312, 1498 (2006).
- ³⁴ Reversal of quantum jumps have been theoretically considered in different contexts, see H. Mabuchi and P. Zoller, Phys. Rev. Lett. 76, 3108 (1996) and R. Ruskov, A. Mizel, and A. N. Korotkov, Phys. Rev. B 75, 220501(R) (2007).
- ³⁵ Florent Lecocq, Ioan M Pop, Zhihui Peng, Iulian Matei, Thierry Crozes, Thierry Fournier, Cécile Naud, Wiebke Guichard, and Olivier Buisson, “Junction fabrication by shadow evaporation without a suspended bridge,” Nanotechnology **22**, 315302 (2011), arXiv:1101.4576.
- ³⁶ Chad T Rigetti, *Quantum Gates for Superconducting Qubits*, Ph.D. thesis, Yale University (2009).
- ³⁷ Z.K. Minev et al., in prep.
- ³⁸ J M Chow, L DiCarlo, J M Gambetta, F Motzoi, L Frunzio, S M Girvin, and R J Schoelkopf, “Optimized driving of superconducting artificial atoms for improved single-qubit gates,” Physical Review A **82**, 040305 (2010).
- ³⁹ M D Reed, *Entanglement and Quantum Error Correction with Superconducting Qubits*, Ph.D. thesis, Yale University (2013).
- ⁴⁰ Jonas Bylander, Simon Gustavsson, Fei Yan, Fumiki Yoshihara, Khalil Harrabi, George Fitch, David G Cory, Yasunobu Nakamura, Jaw-Shen Tsai, and William D Oliver, “Noise spectroscopy through dynamical decoupling with a superconducting flux qubit,” Nature Physics **7**, 565–570 (2011).
- ⁴¹ C Eichler, C Lang, J M Fink, J Govenius, S Filipp, and A Wallraff, “Observation of Entanglement between Itinerant Microwave Photons and a Superconducting Qubit,” Physical Review Letters **109**, 240501 (2012).
- ⁴² Homepage: www.zlatko-minev.com.
- ⁴³ Yehan Liu, *Quantum Feedback Control of Multiple Superconducting Qubits*, Ph.D. thesis, Yale University (2016).
- ⁴⁴ D Ristè, C C Bultink, K W Lehnert, and L DiCarlo, “Feedback Control of a Solid-State Qubit Using High-Fidelity Projective Measurement,” Physical Review Letters **109**, 240502 (2012).
- ⁴⁵ Z. K. Minev, K. Serniak, I. M. Pop, Z. Leghtas, K. Sliwa, M. Hatridge, L. Frunzio, R. J. Schoelkopf, and M. H. Devoret, “Planar Multilayer Circuit Quantum Electrodynamics,” Physical Review Applied **5** (2016), 10.1103/PhysRevApplied.5.044021, arXiv:1509.01619.

- ⁴⁶ Simon E Nigg, Hanhee Paik, Brian Vlastakis, Gerhard Kirchmair, S Shankar, Luigi Frunzio, M H Devoret, R J Schoelkopf, and S M Girvin, “Black-Box Superconducting Circuit Quantization,” *Physical Review Letters* **108**, 240502 (2012).
- ⁴⁷ D H Slichter, R Vijay, S J Weber, S Boutin, M Boissonneault, J M Gambetta, A Blais, and I Siddiqi, “Measurement-Induced Qubit State Mixing in Circuit QED from Up-Converted Dephasing Noise,” *Physical Review Letters* **109**, 153601 (2012).
- ⁴⁸ Daniel Sank, Zijun Chen, Mostafa Khezri, J Kelly, R Barends, B Campbell, Y Chen, B Chiaro, A Dunsworth, A Fowler, E Jeffrey, E Lucero, A Megrant, J Mutus, M Neeley, C Neill, P. J. J. O’Malley, C Quintana, P Roushan, A Vainsencher, T White, J Wenner, Alexander N Korotkov, and John M Martinis, “Measurement-Induced State Transitions in a Superconducting Qubit: Beyond the Rotating Wave Approximation,” *Physical Review Letters* **117**, 190503 (2016).
- ⁴⁹ Maxime Boissonneault, J M Gambetta, and Alexandre Blais, “Dispersive regime of circuit QED: Photon-dependent qubit dephasing and relaxation rates,” *Physical Review A* **79**, 013819 (2009).
- ⁵⁰ R. J. Cook and H. J. Kimble, *Physical Review Letters* **54**, 1023 (1985).
- ⁵¹ R. Dum, P. Zoller, and H. Ritsch, *Physical Review A* **45**, 4879 (1992).
- ⁵² M. Purraiti and S. Putterman, *Physical Review A* **36**, 929 (1987).

II. EXTENDED FIGURES



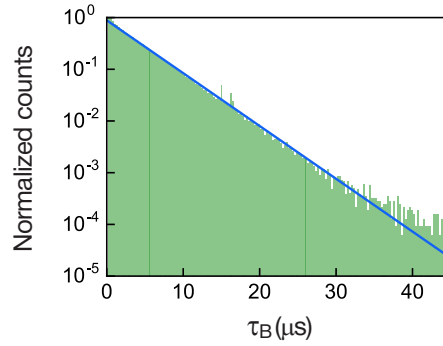
Extended Data Figure 1. Experiment flow. **a**, Flowchart representing the steps of the catch and reverse protocol. Start: internal memory registers are set to zero^{21,43}, including the no-click counter “cnt,” defined below. Prepare B: controller deterministically prepares the atom in $|B\rangle$, a maximally conservative initial state, with measurement-based feedback⁴⁴. Initialize: controller turns on the atom (Ω_{BG} and Ω_{DG}) and cavity (R) drives and begins demodulation. Monitor and catch Δt_{on} : with all drives on (Ω_{BG} , Ω_{DG} , and R), the controller actively monitors the cavity output signal until it detects no-clicks for duration Δt_{on} , as described in panel (b), whereafter the controller proceeds to “monitor and catch Δt_{off} ” in the case that $\Delta t_{off} > 0$; otherwise, for $\Delta t_{off} = 0$, the controller proceeds to “tomography” (“feedback pulse”) for the catch (reverse) protocol. Monitor and catch Δt_{off} : with the Rabi drive Ω_{DG} off, while keeping the drives Ω_{BG} and R on, the controller contin-

ues to monitor the output signal. The controller exits the routine only if it detects a click, proceeding to the “declare B” step of the “monitor and catch Δt_{on} ” routine, or if no further clicks are detected for the pre-defined duration Δt_{off} , proceeding to “tomography” (“feedback pulse”) for the catch (reverse) protocol. Feedback pulse: with all the continuous drives turned off, the controller performs a pulse on the DG transition of the atom, defined by the two angles $\{\theta_I(\Delta t_{\text{catch}}), \varphi_I(\Delta t_{\text{catch}})\}$. Tomography: controller performs next-in-order tomography sequence (see Methods) while the demodulator finishes processing the final data in its pipeline. Advance tomo.: tomography sequence counter is incremented, and after a 50 μs delay, the next realization of the experiment is started. **b**, Concurrent-programming flow chart representation of the “monitor and catch Δt_{on} ” routine. Displayed are the master and demodulator modules of the controller. The demodulator outputs a pair of 16 bit signed integers, $\{I_{\text{rec}}, Q_{\text{rec}}\}$, every $T_{\text{int}} = 260$ ns, which is routed to the master module, as depicted by the large left-pointing arrow. The master module implements the IQ filter (see Methods) and tracks the number of consecutive not- $|B\rangle$ measurement results with the counter cnt. The counter thus keeps track of the no-click time elapsed since the last click, which is understood as a change in the measurement result from $|B\rangle$ to not- $|B\rangle$. When the counter reaches the critical value N_{on} , corresponding to Δt_{on} , the master and demodulator modules synchronously exit the current routine, see the T* branch of the “declare not-B” decision block. Until this condition is fulfilled (F*), the two modules proceed within the current routine as depicted by the black flowlines. To minimize latency and maximize computation throughput, the master and demodulator were designed to be independent sequential processes running concurrently on the FPGA controller, communicating strictly through synchronous message passing, which imposed stringent synchronization and execution time constraints. All master inter-module logic was constrained to run at a 260 ns cycle, the start of which necessarily was imposed to coincide with a “receive & stream record” operation, here, denoted by the stopwatch. In other words, this imposed the algorithmic constraint that all flowchart paths staring at a stopwatch and ending in a stopwatch, itself or other, were constrained to a 260 ns execution timing. A second key timing constraint was imposed by the time required to propagate signals between the different FPGA cards, which corresponded to a minimum branching-instruction duration of 76 ns. **c**, Concurrent-programming flow chart of the master module in the “monitor and catch Δt_{off} ” routine. The corresponding demodulation-module flowchart is identical to that shown of panel (b); hence, it is not

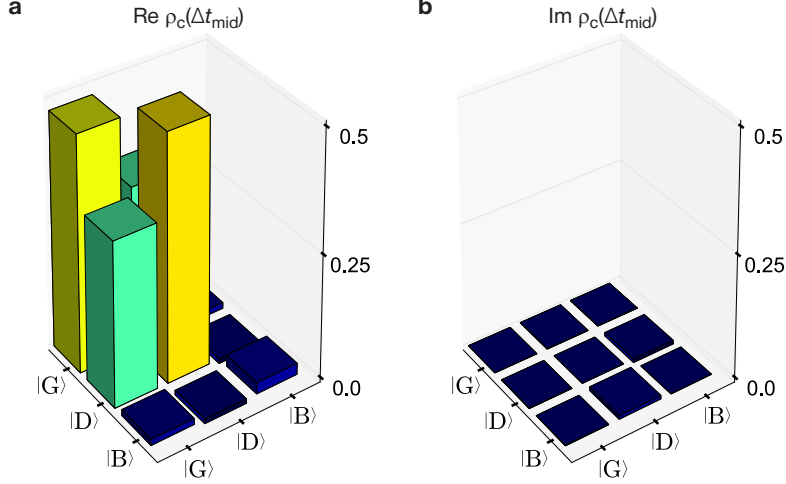
shown. This routine functions in following manner: If a $|B\rangle$ outcome is detected, the controller jumps to the “declare B” block of the monitor & catch Δt_{on} routine; otherwise, when only not- $|B\rangle$ outcomes are observed, and the counter reaches the critical value N_{off} , corresponding to $\Delta t_{\text{catch}} = \Delta t_{\text{on}} + \Delta t_{\text{off}}$, the controller exits the routine.

Symbol	Value	Description
Γ^{-1}	$\approx 8.8 \text{ ns}$	Effective measurement time of $ B\rangle$, approximately given by $1/\kappa\bar{n}$, where $\bar{n} = 5 \pm 0.2$ in the main experiment (see Supplement)
κ^{-1}	$44.0 \pm 0.06 \text{ ns}$	Readout cavity lifetime
T_{int}	260.0 ns	Integration time of the measurement record, set in the controller at the beginning of the experiment
Γ_{BG}^{-1}	$0.99 \pm 0.06 \mu\text{s}$	Average time the atom rests in $ G\rangle$ before an excitation to $ B\rangle$, see Fig. 2b
Δt_{mid}	$3.95 \mu\text{s}$	No-click duration for reaching $Z_{\text{GD}} = 0$ in the flight of the quantum jump from $ G\rangle$ to $ D\rangle$, in the full presence of Ω_{DG} , see Fig. 3b
Γ_{GD}^{-1}	$30.8 \pm 0.4 \mu\text{s}$	Average time the atom stays in $ D\rangle$ before returning to $ G\rangle$ and being detected, see Fig. 2b
T_1^{D}	$116 \pm 5 \mu\text{s}$	Energy relaxation time of $ D\rangle$
$T_{2\text{R}}^{\text{D}}$	$120 \pm 5 \mu\text{s}$	Ramsey coherence time of $ D\rangle$
$T_{2\text{E}}^{\text{D}}$	$162 \pm 6 \mu\text{s}$	Echo coherence time of $ D\rangle$
Γ_{DG}^{-1}	$220 \pm 5 \mu\text{s}$	Average time between two consecutive $ G\rangle$ to $ D\rangle$ jumps

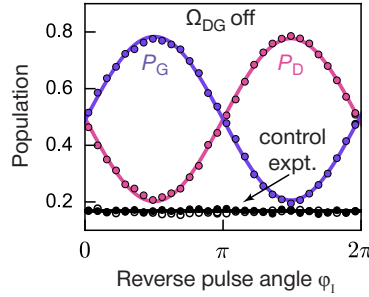
Extended Data Table I. Summary of timescales.



Extended Data Figure 2. Waiting time to switch from a $|B\rangle$ to not- $|B\rangle$ state assignment result. Semi-log plot of the histogram (shaded green) of the duration of times corresponding to $|B\rangle$ -measurement results, τ_B , for 3.2 s of continuous data of the type shown in Fig. 2a. Solid line is an exponential fit, which yields a $4.2 \pm 0.03 \mu\text{s}$ time constant.



Extended Data Figure 3. Mid-flight tomogram. The plots show the real (a) and imaginary (b) parts of the conditional density matrix, ρ_c , at the mid flight of the quantum jump ($\Delta t_{\text{catch}} = \Delta t_{\text{mid}}$), in the presence of the Rabi drive from $|G\rangle$ to $|D\rangle$ ($\Delta t_{\text{off}} = 0$). The population of the $|B\rangle$ state is 0.023, and the magnitude of all imaginary components is less than 0.007.



Extended Data Figure 4. Reversing the quantum jump mid-flight in the absence of Ω_{DG} . Success probabilities P_G (purple) and P_D (orange) to reverse to $|G\rangle$ and complete to $|D\rangle$ the quantum jump mid-flight at $\Delta t_{\text{catch}} = \Delta t'_{\text{mid}}$, defined in Fig. 3b, in the absence of the Rabi drive Ω_{DG} , where $\Delta t_{\text{on}} = 2\mu\text{s}$ and $\theta_1 = \pi/2$. Black dots: success probability for $|G\rangle$ (closed dots) and $|D\rangle$ (open dots) for the control experiment where the intervention is applied at random times, see Fig. 4b.

III. EXPERIMENTAL METHODS

A. Setup

Setup and signals. Our experiments were carried out in a cryogen-free dilution refrigerator (*Oxford Triton 200*). The cavity and JPC were shielded from stray magnetic fields by a cryogenic μ -metal (*Amumetal A4K*) shield. Our input-output cryogenic setup is nearly identical to that described in Ref. 21, aside from the differences evident in the schematic of our setup (see Fig. 1b and Methods) or described in the following.

The control tones depicted in Fig. 1 (also, see Methods) were each generated from in-

dividual microwave generators (Ω_D and Ω_{B0} : *Agilent N5183A*; readout cavity tone R and Ω_{B1} : *Vaunix LabBrick LMS-103-13* and *LMS-802-13*, respectively). To achieve IQ control, the generated tones were mixed (*Marki Microwave Mixers IQ-0618LXP* for the cavity and *IQ-0307LXP* for Ω_{B0}, Ω_{B1} , and Ω_D) with intermediate-frequency (IF) signals synthesized by the 16 bit digital-to-analog converters (DACs) of the integrated FPGA controller system (*Innovative Integration VPXI-ePC*). Prior to mixing, each analog output was filtered by a $50\ \Omega$ low pass filter (*Mini-Circuits BLP-300+*) and attenuated by a minimum of 10 dB. The radio-frequency (RF) output was amplified at room temperature (*MiniCircuits ZVA-183-S+*) and filtered by *Mini-Circuits* coaxial bandpass filters. The output signal was further pulse modulated by the FPGA with high isolation SPST switches (*Analog Device HMC-C019*), which provided additional 80 dB isolation when the control drives were turned off. The signals were subsequently routed to the input lines of the refrigerator, whose details were described in Refs. 21 and 45.

At room temperature, following the cryogenic high-electron mobility amplifier (HEMT; *Low Noise Factory LNF-LNC7-10A*), the signal were amplified by 28 dB (*Miteq AFS3-00101200-35-ULN*) before being mixed down (*Marki image reject double-balanced mixer IRW-0618*) to an intermediate frequency (IF) of 50 MHz, where they were band-pass filtered (*Mini-Circuits SIF-50+*) and further amplified by a cascaded preamplifier (*Stanford Research Systems SR445A*), before finally digitization by the FPGA analog-to-digital converters (ADC).

Device fabrication. See Methods.

B. System characterization

Hamiltonian of the device. The two-transmon, single-readout-cavity system is well described, in the low-excitation manifold, by the approximate dispersive Hamiltonian^{37,46}:

$$\begin{aligned} \hat{H}/\hbar = & \omega_B \hat{b}^\dagger \hat{b} - \frac{1}{2} \alpha_B \hat{b}^{\dagger 2} \hat{b}^2 + \omega_D \hat{d}^\dagger \hat{d} - \frac{1}{2} \alpha_D \hat{d}^{\dagger 2} \hat{d}^2 - \chi_{DB} \hat{b}^\dagger \hat{b} \hat{d}^\dagger \hat{d} \\ & + \left(\omega_C + \chi_B \hat{b}^\dagger \hat{b} + \chi_D \hat{d}^\dagger \hat{d} \right) \hat{c}^\dagger \hat{c}, \end{aligned} \quad (1)$$

where ω_C , ω_B and ω_D are the cavity, bright, and dark qubit transition frequencies, \hat{c} , \hat{b} and \hat{d} are the associated ladder operators, and α and χ are the modal anharmonicities and dispersive shifts, respectively. The states $|B\rangle$ and $|D\rangle$ correspond to one excitation in the bright ($\hat{b}^\dagger |0\rangle$) and dark ($\hat{d}^\dagger |0\rangle$) modes, respectively. The measured parameters of the device and the mode coherences are summarized in Table S2.

DG coherence & tomography control. In Fig. S1, we show the results of a control experiment where we verified the Ramsey coherence (T_{2R}^D) and energy relaxation (T_1^D) times of the DG transition with our tomography method. Solid lines are fitted theoretical curves for the free evolution of the prepared initial state $\frac{1}{\sqrt{2}}(|D\rangle - |G\rangle)$. The $T_{2R}^D = 119.2\ \mu\text{s}$ value gained from the simultaneous fit of $X_{DG}(t)$ and $Y_{DG}(t)$ matches the lifetime independently obtained from a standard T_{2R} measurement. Similarly, the value of $T_1^D = 115.4\ \mu\text{s}$ extracted from an exponential fit of $Z_{DG}(t)$ matches the value obtained from a standard T_1 measurement. We note that our tomography procedure is well calibrated and skew-free, as evident in the zero steady-state values of X_{DG} and Y_{DG} . The steady state Z_{DG} corresponds to the thermal population of the dark state n_{th}^D .

Readout cavity	BG transition	DG transition
Mode frequencies and non-linear parameters		
$\omega_{\text{C}}/2\pi = 8979.640 \text{ MHz}$	$\omega_{\text{BG}}/2\pi = 5570.349 \text{ MHz}$	$\omega_{\text{DG}}/2\pi = 4845.255 \text{ MHz}$
	$\chi_{\text{B}}/2\pi = -5.08 \pm 0.2 \text{ MHz}$	$\chi_{\text{D}}/2\pi = -0.33 \pm 0.08 \text{ MHz}$
	$\alpha_{\text{B}}/2\pi = 195 \pm 2 \text{ MHz}$	$\alpha_{\text{D}}/2\pi = 152 \pm 2 \text{ MHz}$
	$\chi_{\text{DB}}/2\pi = 61 \pm 2 \text{ MHz}$	
Coherence related parameters		
$\kappa/2\pi = 3.62 \pm 0.05 \text{ MHz}$	$T_1^{\text{B}} = 28 \pm 2 \mu\text{s}$	$T_1^{\text{D}} = 116 \pm 5 \mu\text{s}$
$\eta = 0.33 \pm 0.03$	$T_{2\text{R}}^{\text{B}} = 18 \pm 1 \mu\text{s}$	$T_{2\text{R}}^{\text{D}} = 120 \pm 5 \mu\text{s}$
$T_{\text{int}} = 260.0 \text{ ns}$	$T_{2\text{E}}^{\text{B}} = 25 \pm 2 \mu\text{s}$	$T_{2\text{E}}^{\text{D}} = 162 \pm 6 \mu\text{s}$
$n_{\text{th}}^{\text{C}} \leq 0.0017 \pm 0.0002$	$n_{\text{th}}^{\text{B}} \leq 0.01 \pm 0.005$	$n_{\text{th}}^{\text{D}} \leq 0.05 \pm 0.01$
Drive amplitude and detuning parameters		
$\bar{n} = 5.0 \pm 0.2$	$\Omega_{\text{B0}}/2\pi = 1.2 \pm 0.01 \text{ MHz}$	$\Omega_{\text{DG}}/2\pi = 20 \pm 2 \text{ kHz}$
	$\Omega_{\text{B1}}/2\pi = 600 \pm 10 \text{ kHz}$	
$\Delta_{\text{R}} = \chi_{\text{B}}$	$\Delta_{\text{B1}}/2\pi = -30.0 \text{ MHz}$	$\Delta_{\text{DG}}/2\pi = -275.0 \text{ kHz}$

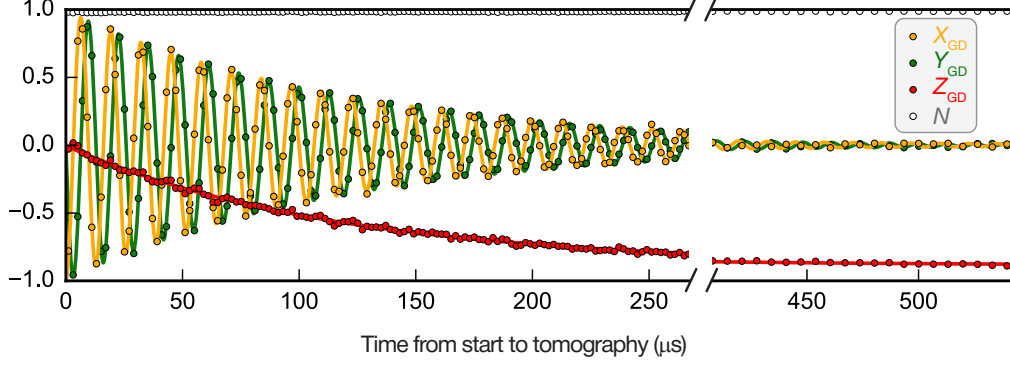
Supplementary Table S2. Compilation of the experimental parameters.

Measurement-induced energy relaxation $T_1(\bar{n})$. Figure S2 shows a characterization of the parasitic measurement-induced energy relaxation of $|B\rangle$ and $|D\rangle$. As is the case in standard cQED systems^{31,47,48}, the $|B\rangle$ level shows strong T_1 degradation⁴⁹ as a function of the readout drive strength \bar{n} . However, the lifetime of the dark state ($|D\rangle$) is protected, and remains largely unaffected even at large drive strengths ($\bar{n} \approx 50$).

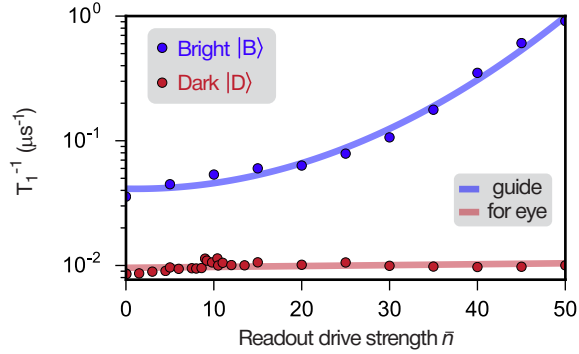
IV. QUANTUM TRAJECTORY THEORY

A. Fluorescence monitored by photon counts

Coherent Bright drive. The experiments with trapped ions¹⁻³ monitor intermittent fluorescence from the bright state $|B\rangle$ to track jumps between $|G\rangle$ and $|D\rangle$.⁵⁰ In the simplest three-level scheme,³ and using coherent radiation to excite both transitions, the master equation for the reduced density operator ρ of the three-level system, written in the interaction



Supplementary Figure S1. Control experiment: time-resolved tomogram of the free evolution of a DG superposition. The atom is prepared in $\frac{1}{\sqrt{2}}(|D\rangle - |G\rangle)$ and tomography is performed after a varied delay. Dots: reconstructed conditional GD tomogram (X_{DG} , Y_{DG} , and Z_{DG}) and population in DG manifold, N (see Methods). Solid lines: theoretical fits.



Supplementary Figure S2. Measurement-induced energy relaxation $T_1(\bar{n})$. Energy relaxation rate (T_1^{-1}) of $|B\rangle$ (blue dots) and $|D\rangle$ (red dots) as a function of \bar{n} , measured with the following protocol: after the atom is prepared in either $|B\rangle$ or $|D\rangle$, the readout tone (R) is turned on for duration t_{read} with amplitude \bar{n} (corresponding to the number of steady-state photons in the readout cavity when excited on resonance), whereafter the population of the initial state is measured. As in all other experiments, the readout drive is applied at the $|B\rangle$ cavity frequency ($\omega_C - \chi_B$). The relaxation rates are extracted from exponential fits of the population decay as a function of t_{read} , from 1.3×10^7 experimental realizations. The solids lines are guides to the eye: blue line indicates the rapid degradation of T_1^B as a function of the readout strength, while the red line indicates the nearly constants T_1^D of the protected dark level.

picture, is

$$\frac{d\rho}{dt} = (i\hbar)^{-1}[H_{\text{drive}}, \rho] + \gamma_B \mathcal{L}[|G\rangle\langle B|]\rho + \gamma_D \mathcal{L}[|G\rangle\langle D|]\rho, \quad (2)$$

where $\mathcal{L}[\xi] \cdot = \xi \cdot \xi^\dagger - \frac{1}{2}\{\xi^\dagger \xi, \cdot\}$ denotes the Lindblad superoperator, γ_B and γ_D are radiative decay rates, and

$$H_{\text{drive}} = i\hbar \frac{\Omega_{BG}}{2} (|B\rangle\langle G| - |G\rangle\langle B|) + i\hbar \frac{\Omega_{DG}}{2} (|D\rangle\langle G| - |G\rangle\langle D|), \quad (3)$$

with Ω_{BG} and Ω_{DG} the Rabi drives. The quantum trajectory description^{4,6,51} unravels ρ into an ensemble of pure states whose ket vectors evolve along stochastic paths conditioned on the clicks of imaginary photon detectors that monitor fluorescence from $|B\rangle$ (and much less frequently from $|D\rangle$). In recognition of each click the ket vector is reset to $|G\rangle$, while otherwise it follows a deterministic evolution as a coherent superposition,

$$|\psi(\Delta t_{\text{catch}})\rangle = C_G(\Delta t_{\text{catch}})|G\rangle + C_B(\Delta t_{\text{catch}})|B\rangle + C_D(\Delta t_{\text{catch}})|D\rangle, \quad (4)$$

where $C_G(0) = 1$, $C_B(0) = C_D(0) = 0$, with $\Delta t_{\text{catch}} = 0$ marking the time of the last click reset, and

$$i\hbar \frac{d|\psi\rangle}{d\Delta t_{\text{catch}}} = \left(H_{\text{drive}} - i\hbar \frac{\gamma_B}{2} |B\rangle\langle B| - i\hbar \frac{\gamma_D}{2} |D\rangle\langle D| \right) |\psi\rangle. \quad (5)$$

The norm of the ket $|\psi(\Delta t_{\text{catch}})\rangle$ is not preserved, but rather gives the probability that the evolution will continue, with no interruption by further clicks, up to time Δt_{catch} ; clearly it must decay with this probability to zero. If we then define

$$W_{DG}(\Delta t_{\text{catch}}) \equiv \frac{C_D(\Delta t_{\text{catch}})}{C_G(\Delta t_{\text{catch}})}, \quad (6)$$

the *normalized* ket vector in the GD-subspace has Bloch vector components

$$Z_{GD}(\Delta t_{\text{catch}}) = \frac{W_{DG}(\Delta t_{\text{catch}}) - W_{DG}^{-1}(\Delta t_{\text{catch}})}{W_{DG}(\Delta t_{\text{catch}}) + W_{DG}^{-1}(\Delta t_{\text{catch}})}, \quad (7)$$

$$X_{GD}(\Delta t_{\text{catch}}) = \frac{2}{W_{DG}(\Delta t_{\text{catch}}) + W_{DG}^{-1}(\Delta t_{\text{catch}})}, \quad (8)$$

$$Y_{GD}(\Delta t_{\text{catch}}) = 0, \quad (9)$$

where, using Eqs. (4) and (5),

$$\frac{d}{d\Delta t_{\text{catch}}} \begin{pmatrix} C_G \\ C_B \\ C_D \end{pmatrix} = \frac{1}{2} \begin{pmatrix} 0 & -\Omega_{BG} & -\Omega_{DG} \\ \Omega_{BG} & -\gamma_B & 0 \\ \Omega_{DG} & 0 & -\gamma_D \end{pmatrix} \begin{pmatrix} C_G \\ C_B \\ C_D \end{pmatrix}. \quad (10)$$

In general this 3×3 system does not have a closed solution in simple form, although there is a particularly simple solution under conditions that produce intermittent fluorescence, i.e., rare jumps from $|G\rangle$ to $|D\rangle$ (“shelving” in the dark state¹) interspersed as intervals of fluorescence “off” in a background of fluorescence “on”. The conditions follow naturally if $|D\rangle$ is a metastable state,¹⁻³ whose lifetime γ_D^{-1} is extremely long on the scale of the mean time, $(\Omega_{BG}^2/2\gamma_B)^{-1}$, between photon detector clicks for a weak Ω_{BG} Rabi drive. Thus, for

$(\Omega_{\text{DG}}, \gamma_{\text{D}}) \ll \Omega_{\text{BG}}^2/2\gamma_{\text{B}} \ll \gamma_{\text{B}}$, Eq. (10) yields the equation of motion

$$\frac{dW_{\text{DG}}}{d\Delta t_{\text{catch}}} = \frac{\Omega_{\text{BG}}^2}{2\gamma_{\text{B}}} W_{\text{DG}} + \frac{\Omega_{\text{DG}}}{2}, \quad (11)$$

whose solution for the click reset initial condition, $W_{\text{DG}}(0) = 0$, is

$$W_{\text{DG}}(\Delta t_{\text{catch}}) = \frac{\Omega_{\text{DG}}}{\Omega_{\text{BG}}^2/\gamma_{\text{B}}} \left[\exp\left(\frac{\Omega_{\text{BG}}^2}{2\gamma_{\text{B}}} \Delta t_{\text{catch}}\right) - 1 \right], \quad (12)$$

from which a long enough interval with no clicks gives $W_{\text{DG}}(\Delta t_{\text{catch}}) \gg 1$ and leads to the conclusion that the ket vector is $|D\rangle$. The time scale for the transition is Δt_{mid} , defined by $W_{\text{DG}}(\Delta t_{\text{mid}}) = 1$.⁵² Simply inverting this equation produces the formula

$$\Delta t_{\text{mid}} = \left(\frac{\Omega_{\text{BG}}^2}{2\gamma_{\text{B}}}\right)^{-1} \ln\left(\frac{\Omega_{\text{BG}}^2/\gamma_{\text{B}}}{\Omega_{\text{DG}}} + 1\right), \quad (13)$$

but strong monitoring, $\Omega_{\text{BG}}^2/\gamma_{\text{B}} \gg \Omega_{\text{DG}}$, allows the -1 , in Eq. (12), and $+1$, in Eq. (13), to be dropped. Equations (7)–(9), (12), and (13) then provide simple formulas for the continuous, deterministic, and coherent evolution of the completed quantum jump:

$$Z_{\text{GD}}(\Delta t_{\text{catch}}) = \tanh\left[\frac{\Omega_{\text{BG}}^2}{2\gamma_{\text{B}}}(\Delta t_{\text{catch}} - \Delta t_{\text{mid}})\right], \quad (14)$$

$$X_{\text{GD}}(\Delta t_{\text{catch}}) = \text{sech}\left[\frac{\Omega_{\text{BG}}^2}{2\gamma_{\text{B}}}(\Delta t_{\text{catch}} - \Delta t_{\text{mid}})\right], \quad (15)$$

$$Y_{\text{GD}}(\Delta t_{\text{catch}}) = 0. \quad (16)$$

These formulas execute a perfect jump, $Z_{\text{GD}}(\infty) = 1$, $X_{\text{GD}}(\infty) = Y_{\text{GD}}(\infty) = 0$. The ideal arises from the assumed strong monitoring, $\Omega_{\text{DG}} \ll \Omega_{\text{BG}}^2/\gamma_{\text{B}}$. Departures from it can be transparently analyzed by adopting an incoherent Bright drive.

Incoherent Bright drive. If the coherent Rabi drive Ω_{BG} is replaced by an incoherent drive Γ_{BG} , the master equation in the interaction picture becomes

$$\frac{d\rho}{dt} = (i\hbar)^{-1}[H_{\text{drive}}, \rho] + \Gamma_{\text{BG}}\mathcal{L}[|B\rangle\langle G|]\rho + (\gamma_{\text{B}} + \Gamma_{\text{BG}})\mathcal{L}[|G\rangle\langle B|]\rho + \gamma_{\text{D}}\mathcal{L}[|G\rangle\langle D|]\rho, \quad (17)$$

where

$$H_{\text{drive}} = i\hbar\frac{\Omega_{\text{DG}}}{2}(|D\rangle\langle G| - |G\rangle\langle D|). \quad (18)$$

The previous weak drive assumption, $\Omega_{\text{BG}}^2/2\gamma_{\text{B}} \ll \gamma_{\text{B}}$, is now carried over with the assumption $\Gamma_{\text{BG}} \ll \gamma_{\text{B}}$, which says that the time between clicks in fluorescence is essentially the same as the time separating photon absorptions from the incoherent drive, as absorption is rapidly followed by fluorescence ($\gamma_{\text{B}} + \Gamma_{\text{BG}} \gg \Gamma_{\text{BG}}$). This brings a useful simplification, since, following each reset to $|G\rangle$, the unnormalized ket evolves in the GD-subspace,

$$i\hbar\frac{d|\psi\rangle}{d\Delta t_{\text{catch}}} = \left(H_{\text{drive}} - i\hbar\frac{\Gamma_{\text{BG}}}{2}|G\rangle\langle G| - i\hbar\frac{\gamma_{\text{D}}}{2}|D\rangle\langle D|\right)|\psi\rangle, \quad (19)$$

thus replacing Eqs. (10) and (11) by the simpler 2×2 system

$$\frac{d}{d\Delta t_{\text{catch}}} \begin{pmatrix} C_G \\ C_D \end{pmatrix} = \frac{1}{2} \begin{pmatrix} -\Gamma_{BG} & -\Omega_{DG} \\ \Omega_{DG} & -\gamma_D \end{pmatrix} \begin{pmatrix} C_G \\ C_D \end{pmatrix}, \quad (20)$$

and, if $\gamma_D \ll \Gamma_{BG}$, the equation of motion

$$\frac{dW_{DG}}{d\Delta t_{\text{catch}}} = \frac{\Gamma_{BG}}{2} W_{DG} + \frac{\Omega_{DG}}{2} (1 + W_{DG}^2), \quad (21)$$

with solution, for $W_{DG}(0) = 0$,

$$W_{DG}(\Delta t_{\text{catch}}) = \frac{\exp[(V - V^{-1})\Omega_{DG}\Delta t_{\text{catch}}/2] - 1}{V - V^{-1} \exp[(V - V^{-1})\Omega_{DG}\Delta t_{\text{catch}}/2]}, \quad (22)$$

where

$$V = \frac{1}{2} \frac{\Gamma_{BG}}{\Omega_{DG}} + \sqrt{\frac{1}{4} \left(\frac{\Gamma_{BG}}{\Omega_{DG}} \right)^2 - 1}. \quad (23)$$

Inversion of the condition $W_{DG}(\Delta t_{\text{mid}}) = 1$ gives the characteristic time scale

$$\Delta t_{\text{mid}} = 2 [(V - V^{-1})\Omega_{DG}]^{-1} \ln \left(\frac{V + 1}{V^{-1} + 1} \right). \quad (24)$$

Equations (22)–(24) replace Eqs. (12) and (13); although, under strong monitoring ($\Gamma_{BG} \gg \Omega_{DG}$), they revert to these results with the substitution $\Omega_{BG}^2/2\gamma_B \rightarrow \Gamma_{BG}/2$, recovering Eqs. (7)–(9) with the same substitution. More generally, $W_{DG}(\Delta t_{\text{catch}})$ goes to infinity at finite Δt_{catch} , changes sign, and returns from infinity to settle on the steady value $W_{DG}(\infty) = -V$. The singular behavior marks a trajectory passing through the north pole of Bloch sphere. It yields the long-time solution

$$Z_{GD}(\infty) = \sqrt{1 - 4 \left(\frac{\Omega_{DG}}{\Gamma_{BG}} \right)^2}, \quad X_{GD}(\infty) = -2 \frac{\Omega_{DG}}{\Gamma_{BG}}, \quad Y_{GD}(\infty) = 0, \quad (25)$$

in contrast to the perfect jump of Eqs. (14)–(16).

Dark drive off. Turing the Dark drive off shortly after a click reset demonstrates the connection between the flight of a quantum jump and a projective measurement. The only change is the setting of Ω_{DG} to zero at time Δt_{on} on the right-hand side of Eqs. (11) and (21). Subsequently, $W_{DG}(\Delta t_{\text{catch}})$ continues its exponential growth at rate $\Omega_{BG}^2/2\gamma_B$ [Eq. (11)] or $\Gamma_{BG}/2$ [Eq. (21)]. Equations (7)–(9) still hold, but now with

$$\Delta t_{\text{mid}} = \left(\frac{\Omega_{BG}^2}{2\gamma_B}, \frac{\Gamma_{BG}}{2} \right)^{-1} \ln [W_{DG}^{-1}(\Delta t_{\text{on}})]. \quad (26)$$

Further evolution realizes a projective measurement of whether the state is $|G\rangle$ or $|D\rangle$, where the normalized state at Δt_{on} is

$$\frac{|\psi(\Delta t_{\text{on}})\rangle}{\sqrt{\text{Norm}(\Delta t_{\text{on}})}} = \frac{C_G(\Delta t_{\text{on}})|G\rangle + C_D(\Delta t_{\text{on}})|D\rangle}{\sqrt{\text{Norm}(\Delta t_{\text{on}})}}, \quad (27)$$

with $\text{Norm}(\Delta t_{\text{on}}) = C_{\text{G}}^2(\Delta t_{\text{on}}) + C_{\text{D}}^2(\Delta t_{\text{on}})$ the probability for the jump to reach $\Delta t_{\text{catch}} = \Delta t_{\text{on}}$ after a click reset to $|G\rangle$ at $\Delta t_{\text{catch}} = 0$. The probability for the jump to continue to $\Delta t_{\text{catch}} > \Delta t_{\text{on}}$ (given Δt_{on} is reached) is then

$$\frac{\text{Norm}(\Delta t_{\text{catch}})}{\text{Norm}(\Delta t_{\text{on}})} = \frac{C_{\text{D}}^2(\Delta t_{\text{on}})}{\text{Norm}(\Delta t_{\text{on}})} + \frac{C_{\text{G}}^2(\Delta t_{\text{on}})}{\text{Norm}(\Delta t_{\text{on}})} \exp \left[- \left(\frac{\Omega_{\text{BG}}^2}{\gamma_{\text{B}}} \right) \Delta t_{\text{catch}} \right], \quad (28)$$

and, as expected, the probability for the jump to complete—for the measurement to answer $|D\rangle$ —is the probability to occupy state $|D\rangle$ at time Δt_{on} , i.e., $C_{\text{D}}^2(\Delta t_{\text{on}})/\text{Norm}(\Delta t_{\text{on}})$.

B. Bright state monitored by dispersive cavity readout

Stochastic Schrödinger equation. Monitoring the quantum jump through fluorescence photon counts provides a clean and simple way of analyzing the deterministic character of the evolution. It is prohibitively challenging for an experiment, though, as the time origin $\Delta t_{\text{catch}} = 0$ is set by the click reset to $|G\rangle$, and in an ensemble of measurements, all resets must be aligned on the very last click before an interval of deterministic evolution (Eqs. (7)–(9)) in order for Δt_{mid} to be aligned over the ensemble; low detection efficiency—on the order of 10^{-3} or less^{1–3}—in the first ion experiments does not permit this. Monitoring through a dispersive cavity readout provides a robust way of aligning $\Delta t_{\text{catch}} = 0$, hence Δt_{mid} , over an ensemble of measurements. Leaving aside imperfections (see below), the master equation in the interaction picture is

$$\frac{d\rho}{dt} = (i\hbar)^{-1} [H_{\text{drive}}, \rho] + (i\hbar)^{-1} [H_{\text{R}}, \rho] + \kappa \mathcal{L}[\hat{c}] \rho, \quad (29)$$

with

$$H_{\text{drive}} = i\hbar \left[\frac{\Omega_{\text{BG}}(t)}{2} |B\rangle\langle G| - \frac{\Omega_{\text{BG}}^*(t)}{2} |G\rangle\langle B| \right] + i\hbar \frac{\Omega_{\text{DG}}}{2} (|D\rangle\langle G| - |G\rangle\langle D|), \quad (30)$$

and

$$H_{\text{R}} = -\hbar\Delta_{\text{R}}\hat{c}^\dagger\hat{c} + i\hbar\frac{\kappa}{2}\sqrt{\bar{n}}(\hat{c}^\dagger - \hat{c}) + \hbar(\chi_{\text{B}}|B\rangle\langle B| + \chi_{\text{D}}|D\rangle\langle D|)\hat{c}^\dagger\hat{c}, \quad (31)$$

where the bi-chromatic drive $\Omega_{\text{BG}}(t) = \Omega_{\text{B0}} + \Omega_{\text{B1}} \exp(-i\Delta_{\text{B1}}t)$ replaces the Rabi drive Ω_{BG} of Eq. (3), \bar{n} is the mean photon number in the readout cavity when driven on resonance, and Δ_{R} is the detuning of the probe from the unshifted cavity resonance; the bi-chromatic drive facilitates transitions in both directions between $|G\rangle$ and $|B\rangle$, given that the bright level shifts when the cavity fills with photons. The quantum trajectory unraveling monitors the reflected probe with efficiency η and accounts for residual photon loss through random jumps; thus, the stochastic Schrödinger equation combines a continuous evolution (heterodyne readout channel),

$$d|\psi\rangle = \left[\frac{1}{i\hbar} \left(H_{\text{drive}} + H_{\text{R}} - i\hbar\frac{\kappa}{2}\hat{c}^\dagger\hat{c} \right) dt + \sqrt{\eta}\sqrt{\kappa}d\zeta\hat{c} \right] |\psi\rangle, \quad (32)$$

where

$$d\zeta = \sqrt{\eta}\sqrt{\kappa} \frac{\langle\psi|a^\dagger|\psi\rangle}{\langle\psi|\psi\rangle} dt + dZ, \quad (33)$$

dZ a complex Wiener increment, with random jumps (photon loss),

$$|\psi\rangle \rightarrow \hat{c}|\psi\rangle \quad \text{at rate} \quad (1-\eta)\kappa \frac{\langle\psi|\hat{c}^\dagger\hat{c}|\psi\rangle}{\langle\psi|\psi\rangle}. \quad (34)$$

The monitored output $d\zeta$ is scaled—to units of (readout cavity photon number) $^{1/2}$ —and filtered to generate simulated quadratures I_{rec} and Q_{rec} of the measurement record:

$$dI_{\text{rec}} = -\frac{\kappa_{\text{filter}}}{2} \left[I_{\text{rec}} dt - \left(\eta \frac{\kappa}{2} \right)^{-1/2} \text{Re}(d\zeta) \right], \quad (35)$$

$$dQ_{\text{rec}} = -\frac{\kappa_{\text{filter}}}{2} \left[Q_{\text{rec}} dt - \left(\eta \frac{\kappa}{2} \right)^{-1/2} \text{Im}(d\zeta) \right], \quad (36)$$

where κ_{filter} is the bandwidth of the experimental readout amplifier chain.

Independently measured imperfections. The stochastic Schrödinger equation is supplemented by spontaneous and thermal jumps on both the $|G\rangle$ to $|B\rangle$ and $|G\rangle$ to $|D\rangle$ transitions, and by pure dephasing of the GB and GD coherences. With these processes included, the term

$$-i\hbar \left\{ \left[\frac{\gamma_B}{2} (n_{\text{th}}^B + 1) + \gamma_B^\phi \right] |B\rangle\langle B| + \left[\frac{\gamma_D}{2} (n_{\text{th}}^D + 1) + \gamma_D^\phi \right] |D\rangle\langle D| + \frac{\gamma_B n_{\text{th}}^B + \gamma_D n_{\text{th}}^D}{2} |G\rangle\langle G| \right\}$$

is added to the non-Hermitian Hamiltonian $H_{\text{drive}} + H_R - i\hbar(\kappa/2)\hat{c}^\dagger\hat{c}$ on the right-hand side of Eq. (32), and there are additional random jumps

$$|\psi\rangle \rightarrow |G\rangle \quad \text{at rate} \quad \gamma_B (n_{\text{th}}^B + 1) \frac{\langle\psi|B\rangle\langle B|\psi\rangle}{\langle\psi|\psi\rangle} + \gamma_D (n_{\text{th}}^D + 1) \frac{\langle\psi|D\rangle\langle D|\psi\rangle}{\langle\psi|\psi\rangle}, \quad (37)$$

$$|\psi\rangle \rightarrow |B\rangle \quad \text{at rate} \quad \gamma_B n_{\text{th}}^B \frac{\langle\psi|G\rangle\langle G|\psi\rangle}{\langle\psi|\psi\rangle} + 2\gamma_B^\phi \frac{\langle\psi|B\rangle\langle B|\psi\rangle}{\langle\psi|\psi\rangle}, \quad (38)$$

$$|\psi\rangle \rightarrow |D\rangle \quad \text{at rate} \quad \gamma_D n_{\text{th}}^D \frac{\langle\psi|G\rangle\langle G|\psi\rangle}{\langle\psi|\psi\rangle} + 2\gamma_D^\phi \frac{\langle\psi|D\rangle\langle D|\psi\rangle}{\langle\psi|\psi\rangle}. \quad (39)$$

The parameters $\gamma_{B,D}$, $n_{\text{th}}^{B,D}$, and $\gamma_{B,D}^\phi$ are mapped to the independently measured parameters $T_{B,D}^1$, $n_{\text{th}}^{G,D}$, and $T_{2R}^{B,D}$ listed in Table S2 (see below).

Leakage from the GBD-manifold. The three-state manifold, $|G\rangle$, $|B\rangle$, and $|D\rangle$, is not strictly closed. Rare transitions to higher excited states of the two-transmon system may occur. This possibility is included with the addition of the further term

$$-i\hbar \left\{ \frac{\gamma_{FG}}{2} |G\rangle\langle G| + \frac{\gamma_{FD}}{2} |D\rangle\langle D| + \frac{\gamma_{GF} + \gamma_{DF}}{2} |F\rangle\langle F| \right\}$$

to the non-Hermitian Hamiltonian, and the associated additional random jumps,

$$|\psi\rangle \rightarrow |F\rangle \quad \text{at rate} \quad \gamma_{FG} \frac{\langle\psi|G\rangle\langle G|\psi\rangle}{\langle\psi|\psi\rangle} + \gamma_{FD} \frac{\langle\psi|D\rangle\langle D|\psi\rangle}{\langle\psi|\psi\rangle}, \quad (40)$$

$$|\psi\rangle \rightarrow |G\rangle \quad \text{at rate} \quad \gamma_{GF} \frac{\langle\psi|F\rangle\langle F|\psi\rangle}{\langle\psi|\psi\rangle}, \quad (41)$$

$$|\psi\rangle \rightarrow |D\rangle \quad \text{at rate} \quad \gamma_{DF} \frac{\langle\psi|F\rangle\langle F|\psi\rangle}{\langle\psi|\psi\rangle}, \quad (42)$$

where $|F\rangle$ is a single catch-all higher excited state.

V. COMPARISON BETWEEN EXPERIMENT AND THEORY

A. Simulated data sets

Independently measured parameters. The parameters used in the simulations are listed in Table S3. In most cases they are set to the value at the center of the range quoted in Table S2, but with three exceptions: (i) T_1^B and T_1^D are set to lower values in response to the photon number dependence of the readout displayed in Fig. S2; (ii) $\Omega_{DG}/2\pi$ is set higher, but still falls inside the experimental error bars, and (iii) $n_{th}^C = 0$. Of the three exceptions, only $\Omega_{DG}/2\pi$ has a noticeable effect on the comparison between simulated and experimental data sets.

Leakage from the GBD-manifold. Additional random jumps to state $|F\rangle$ are governed by four parameters that are not independently measured; they serve as fitting parameters, required to bring the simulation into agreement with the asymptotic behavior of $Z(\Delta t_{catch})$, which, without leakage to $|F\rangle$, settles to a value higher than is measured in the experiment. The evolution of the $X(\Delta t_{catch})$ is largely unaffected by the assignment of these parameters, where any change that does occur can be offset by adjusting $\Omega_{DG}/2\pi$ while staying within the experimental error bars.

Ensemble average. Simulated data sets are computed as an ensemble average by sampling an ongoing Monte Carlo simulation, numerically implementing the model outlined in Eqs. (32)–(42). Quadratures I_{rec} and Q_{rec} are computed from Eqs. (35) and (36), digitized with integration time $T_{int} = 260\text{ns}$, and then, as in the experiment, a hysteric filter is used to locate “click” events ($\Delta t_{catch} = 0$) corresponding to an inferred change of state from $|B\rangle$ to not- $|B\rangle$. During the subsequent sampling interval ($\Delta t_{catch} \geq 0$), the four quantities

$$(Z_{GD}^j, X_{GD}^j, Y_{GD}^j, P_{BB}^j)(\Delta t_{catch}) = (Z_{GD}^{rec}, X_{GD}^{rec}, Y_{GD}^{rec}, P_{BB}^{rec})(t_j + \Delta t_{catch}), \quad (43)$$

Readout cavity	BG transition	DG transition
Non-linear parameters		
	$\chi_B/2\pi = -5.08 \text{ MHz}$	$\chi_D/2\pi = -0.33 \text{ MHz}$
Coherence related parameters		
$\kappa/2\pi = 3.62 \text{ MHz}$	$T_1^B = 15 \mu\text{s}$	$T_1^D = 105 \mu\text{s}$
$\eta = 0.33$	$T_2^B = 18 \mu\text{s}$	$T_2^D = 120 \mu\text{s}$
$T_{\text{int}} = 260.0 \text{ ns}$		
$n_{\text{th}}^C = 0$	$n_{\text{th}}^B = 0.01$	$n_{\text{th}}^D = 0.05$
Drive amplitude and detuning parameters		
$\bar{n} = 5.0$	$\Omega_{B0}/2\pi = 1.2 \text{ MHz}$	$\Omega_{DG}/2\pi = 21.6 \text{ kHz}$
	$\Omega_{B1}/2\pi = 600 \text{ kHz}$	
$\Delta_R = \chi_B$	$\Delta_{B1}/2\pi = -30.0 \text{ MHz}$	$\Delta_{DG}/2\pi = -274.5 \text{ kHz}$

Supplementary Table S3. Compilation of the simulation parameters.

with t_j is the click time and

$$Z_{\text{GD}}^{\text{rec}}(t) = \frac{\langle D|\psi(t)\rangle\langle\psi(t)|D\rangle - \langle G|\psi(t)\rangle\langle\psi(t)|G\rangle}{\langle\psi(t)|\psi(t)\rangle}, \quad (44)$$

$$X_{\text{GD}}^{\text{rec}}(t) + iY_{\text{GD}}^{\text{rec}}(t) = 2\frac{\langle D|\psi(t)\rangle\langle\psi(t)|G\rangle}{\langle\psi(t)|\psi(t)\rangle}, \quad (45)$$

$$P_{\text{BB}}^{\text{rec}}(t) = \frac{\langle B|\psi(t)\rangle\langle\psi(t)|B\rangle}{\langle\psi(t)|\psi(t)\rangle}, \quad (46)$$

are computed, and running sums of each are updated. The sample terminates when the measurement record indicates a change of state from not- $|B\rangle$ back to $|B\rangle$. Finally, for comparison with the experiment, Bloch vector components are recovered from the average over sample intervals via the formula

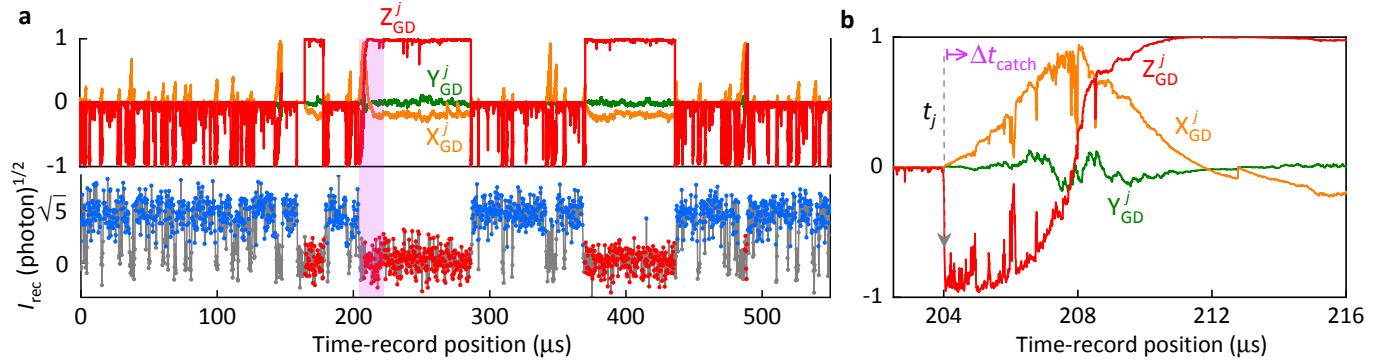
$$(Z_{\text{GD}}, X_{\text{GD}}, Y_{\text{GD}})(\Delta t_{\text{catch}}) = \frac{\sum_j^{N(\Delta t_{\text{catch}})} (Z_{\text{GD}}^j, X_{\text{GD}}^j, Y_{\text{GD}}^j)(\Delta t_{\text{catch}})}{N(\Delta t_{\text{catch}}) - \sum_j^{N(\Delta t_{\text{catch}})} P_{\text{BB}}^j(\Delta t_{\text{catch}})}, \quad (47)$$

where $N(\Delta t_{\text{catch}})$ is the number of sample intervals that extend up to, or beyond, the time Δt_{catch} . The simulation and sampling procedure is illustrated in Fig. S3, and a comparison between the experiment and the simulation is provided in Fig. S4.

B. Error budget

Imperfections. Various imperfections are expected to reduce the maximum coherence recovered in the measurement of $X_{\text{GD}}(\Delta t_{\text{catch}})$. They include:

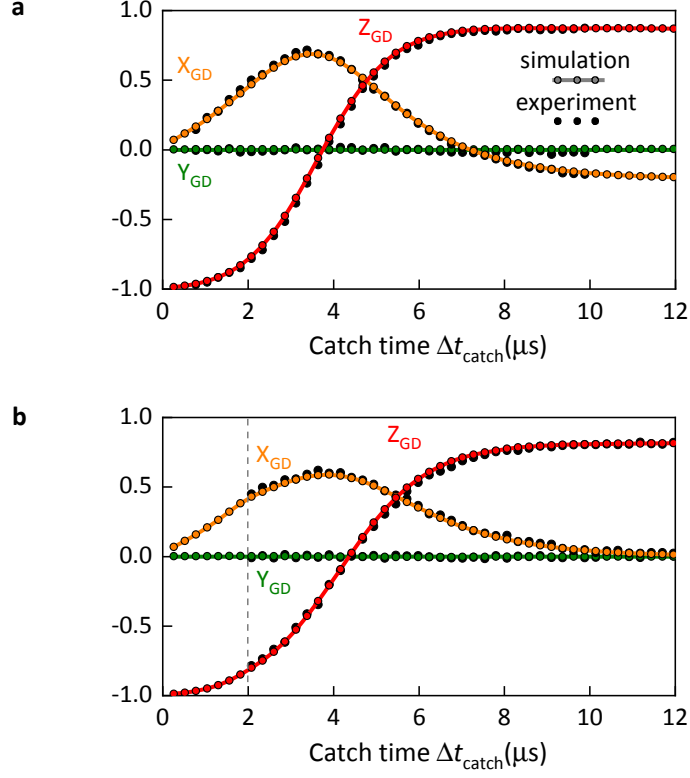
- (i) Readout errors when inferring $|B\rangle$ to not- $|B\rangle$ transitions and the reverse. Such errors



Supplementary Figure S3. Sampling of the Monte-Carlo simulation. **a**, Simulated measurement quadrature I_{rec} and correlated trajectory computed from Eqs. (44) and (45). Three sample intervals are shown. The earliest corresponds to leakage from the GBD-manifold, where a jump from $|G\rangle$ to $|F\rangle$ is followed by a jump from $|F\rangle$ to $|D\rangle$. The second and third sample intervals correspond to direct transitions from $|G\rangle$ to $|D\rangle$, which are continuously monitored and the object of the experiment. **b**, Expanded view of the shaded region of the second sample interval in panel (a). The evolution is continuous but not smooth, due to backaction noise from the continuously monitored readout. This feature is in sharp contrast to the perfect “no-click” readout upon which the simple theory of Sec. IV A is based.

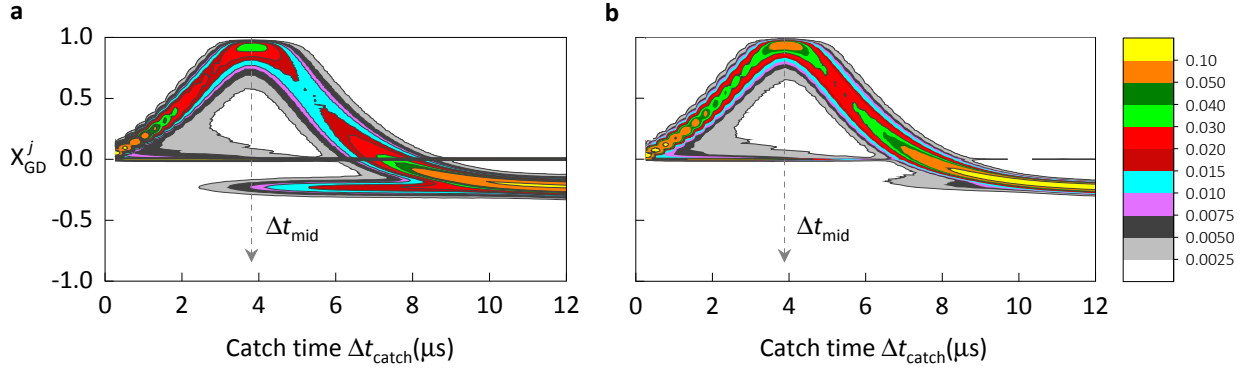
affect the assignment of Δt_{catch} , which can be either too short or too long to correlate correctly with the true state of the system.

- (ii) Leaks from the GBD-manifold to higher excited states. These errors mimic a $|B\rangle$ to not- $|B\rangle$ transition, as in the first sample interval of Fig. S3, yet the anticipated coherent evolution within the GBD-manifold does not occur.
- (iii) Thermal jumps from $|G\rangle$ to $|D\rangle$. Such incoherent transitions contribute in a similar way to $Z_{\text{GD}}(\Delta t_{\text{catch}})$, while making no contribution to the measured coherence.
- (iv) Direct dephasing of the DG-coherence.
- (v) Partial distinguishability of $|G\rangle$ and $|D\rangle$. The readout cavity is not entirely empty of photons when the state is not- $|B\rangle$, in which case the cross-Kerr interaction $\chi_{\text{D}}|D\rangle\langle D|\hat{c}^\dagger\hat{c}$ shifts the Ω_{DG} Rabi drive from resonance; hence, backaction noise is transferred from the photon number to $X_{\text{GD}}(\Delta t_{\text{catch}})$.



Supplementary Figure S4. Comparison between simulation and experiment. **a**, Simulated data set obtained with Rabi drive Ω_{DG} turned on for the entire Δt_{catch} ; parameters taken from Table S3 and leakage from the GBD-manifold included with $(\gamma_{\text{FG}}, \gamma_{\text{FD}})/2\pi = 0.38\text{kHz}$ and $(\gamma_{\text{GF}}, \gamma_{\text{DF}})/2\pi = 11.24\text{kHz}$. **b**, Simulated data set obtained with Rabi drive Ω_{DG} turned off at time $\Delta t_{\text{on}} = 2\mu\text{s}$; parameters taken from Table S3 and leakage from the GBD-manifold included with $\gamma_{\text{FG}}/2\pi = 0.217\text{kHz}$, $\gamma_{\text{FD}}/2\pi = 4.34\text{kHz}$, $\gamma_{\text{GF}}/2\pi = 11.08\text{kHz}$, and $\gamma_{\text{DF}}/2\pi = 15.88\text{kHz}$. When leakage from the GBD-manifold is omitted, the Z_{GD} curve rises more sharply and settles to a value that is 10% (20%) higher in panel (a) (panel (b)).

Budget for lost coherence. The maximum coherence reported in the experiment is 0.71 ± 0.005 . In the simulation it is a little lower at 0.69. By removing the imperfections from the simulation, one by one, we can assign a fraction of the total coherence loss to each. Readout errors are eliminated by identifying transitions between $|B\rangle$ and not- $|B\rangle$ in the ket $|\psi\rangle$ rather than from the simulated measurement record; all other imperfections are turned off by setting some parameter to zero. The largest coherence loss comes from readout errors, whose elimination raises the $X_{\text{GD}}(\Delta t_{\text{catch}})$ maximum by 0.09. The next largest comes from leakage to higher excited states, which raises the maximum by a further 0.06. Setting χ_D to zero adds a further 0.04, and thermal transitions and pure dephasing together add 0.02. Figure S5 illustrates the change in the distribution of $X_{\text{GD}}^j(\Delta t_{\text{catch}})$ samples underlying the recovery of coherence. The removal of the finger pointing to the left in panel (a) is mainly brought about by the elimination of readout errors, while the reduced line of zero coherence marks the elimination of leakage to higher excited states. Aside from these two largest changes, there is also a sharpening of the distribution, at a given Δt_{catch} , when moving from panel (a) to panel (b). Having addressed the five listed imperfections, a further 10% loss remains unaccounted for, i.e., the distribution of panel (b) is not a line passing through $X_{\text{GD}}^j(\Delta t_{\text{mid}}) = 1$. The final 10% is explained by the heterodyne detection backaction noise, a function of the drive and measurement parameters, displayed in panel (b) of Fig. S3.



Supplementary Figure S5. Coherence loss through sample to sample fluctuations.

a, Contour plot of the distribution of $X_{\text{GD}}^j(\Delta t_{\text{catch}})$ samples corresponding to the simulated data set displayed in panel (a) of Fig. S4. **b**, Same as panel (a) but with transitions between $|B\rangle$ and not- $|B\rangle$ identified in the ket $|\psi\rangle$ rather than from the simulated measurement record, and with changed parameters: $(\gamma_{\text{FG}}, \gamma_{\text{FD}}, \gamma_{\text{GF}}, \gamma_{\text{DF}})/2\pi = 0$, $n_{\text{th}}^{\text{B}} = n_{\text{th}}^{\text{D}} = 0$, $T_2^{\text{D}} = 2T_1^{\text{D}}$, and $\chi_D/2\pi = 0$.